Atmospheric Environment 295 (2023) 119530

Contents lists available at ScienceDirect

Atmospheric Environment

journal homepage: www.elsevier.com/locate/atmosenv

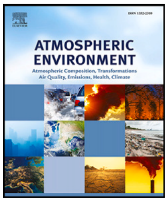

# Disentangling temperature and water stress contributions to trends in isoprene emissions using satellite observations of formaldehyde, 2005–2016

S. Strada [a,*], M. Fernández-Martínez [b,c,d], J. Peñuelas [c,e], M. Bauwens [f], T. Stavrakou [f], A. Verger [c,g], F. Giorgi [a]

[a] *Earth System Physics Section, The Abdus Salam International Centre for Theoretical Physics, Strada Costiera 11, Trieste, 34151, Italy*
[b] *Plants and Ecosystems (PLECO), Department of Biology, Universiteit Antwerpen, BE-2610, Wilrijk, Belgium*
[c] *Centre for Research on Ecology and Forestry Application (CREAF), Cerdanyola del Vallés, Catalonia, 08193, Spain*
[d] *Department of Evolutionary Biology, Ecology and Environmental Sciences, University of Barcelona (BEECA-UB), E08028, Barcelona, Catalonia, Spain*
[e] *Global Ecology Unit, Autonomous University of Barcelona, Spanish National Research Council (CREAF-CSIC-UAB), 08193, Bellaterra, Catalonia, Spain*
[f] *Royal Belgian Institute for Space Aeronomy (BIRA-IASB), Avenue Circulaire 3, Brussels, 1180, Belgium*
[g] *Desertification Research Centre, Spanish National Research Council (CIDE-CSIC), 46113, Valéncia, Spain*

## HIGHLIGHTS

- Using formaldehyde retrievals to probe isoprene trends and the role of drivers.
- Combined effect of temperature and water availability modulate isoprene emissions.
- Water availability sustains isoprene emissions over a dry region such as Australia.
- Isoprene emissions increase under water stress across the Amazon Basin and Europe.
- Mild/short water stress amplifies isoprene emissions while severe/long reduces them.

## ARTICLE INFO

*Keywords:*
Formaldehyde
Isoprene
Temperature
Water availability
Soil moisture
Drought
OMI satellite observations
Generalized linear mixed-effects models

## ABSTRACT

Isoprene, produced by plants in response to multiple drivers, affects climate and air quality when released into the atmosphere. In turn, climate change may influence isoprene emissions through variations in occurrence and intensity of types of stress that affect plant functions. We test the effects of multiple drivers (temperature, precipitation, soil moisture, drought index, biomass, aerosols, burned fraction) on space retrievals of formaldehyde (HCHO) column concentrations, as a proxy for isoprene emissions, at global and regional scales over the period 2005–2016. We find declines in HCHO column concentrations over the study period across Europe, the Amazon Basin, southern Africa, and southern Australia, and increases across India, China, and mainland Southeast Asia. Temporal effects and the interactions among drivers are analyzed using generalized linear mixed-effects models to explain trends in HCHO column concentrations. Results show that HCHO column concentrations increase with temperature at the global scale and across the Amazon Basin and India–China regions, even under low levels of precipitation, provided that sufficient soil moisture can maintain vegetation functions and the associated isoprene emissions. Water availability sustains isoprene emissions in dry regions such as Australia, where HCHO column concentrations are positively associated with mean precipitation, with this relation intensifying at low levels of soil moisture. In contrast, isoprene emissions increase under water stress across the Amazon Basin and Europe, where HCHO column concentrations are negatively associated with levels of soil moisture and drought as calculated by the Standardized Precipitation–Evapotranspiration Index (SPEI). This study confirms the key role of temperature in modulating global and regional isoprene emissions and highlights contrasting regional effects of water stress on these emissions.

---

* Corresponding author.
*E-mail address:* sstrada@ictp.it (S. Strada).

https://doi.org/10.1016/j.atmosenv.2022.119530
Received 5 August 2022; Received in revised form 29 November 2022; Accepted 5 December 2022

## 1. Introduction

Plants produce and emit more than ten thousand types of biogenic volatile organic compounds (BVOCs) (Baldwin, 2010) in response to biotic and abiotic triggers, such as attack by insects, herbivores and pathogens, impacts of radiation, air temperature, nutrient and water availability, carbon dioxide and ozone levels, and land use change (Kesselmeier and Staudt, 1999; Peñuelas and Llusià, 2001; Niinemets et al., 2004; Laothawornkitkul et al., 2009; Fernández-Martínez et al., 2017). Isoprene, which accounts for about 50% of total global BVOC emissions (Guenther et al., 2012), plays an important role in the low troposphere and boundary layer chemistry, due to its abundance and chemical reactivity. Once released into the atmosphere, isoprene influences the levels of greenhouse gases and air pollutants, such as methane, ozone, and aerosols, that subsequently affect climate and air quality (Chameides et al., 1988; Atkinson and Arey, 2003; Pacifico et al., 2009). Global warming and modified precipitation regimes are expected to affect isoprene emissions (Peñuelas and Staudt, 2010) through increases in the occurrence and intensity of severe thermal and water stress that influence plant functions (Meleux et al., 2007; Langner et al., 2012; Churkina et al., 2017); however, the magnitude and sign of the effects of increases in temperature and water stress on isoprene emissions are still poorly known.

While increases in temperature enhance isoprene emissions, effects of water stress are more variable. For example, severe or long-term water stress reduces BVOC emissions, whereas mild or short-term water stress temporarily amplifies or maintains emissions to protect plants against on-going stress (Niinemets, 2009; Peñuelas and Staudt, 2010). A review of studies of BVOC emissions under water stress reported decreases in emissions in 50% of cases, increases in 25%, and no change in the remaining 25% (Peñuelas and Staudt, 2010), with such variability being due to, at least partially, differences in experimental protocol (e.g., intensity and timing of water stress, target biogenic compounds, and plant species). Recent meta-analyses of observational studies of isoprene emissions reported a 23% decrease when relative soil water content drops to 55% (relative to 100% soil water content in the control experiment) (Feng et al., 2019) and no intermediate increase under mild or short-term water stress, in contrast to other BVOCs such as monoterpenes and sesquiterpenes (Bonn et al., 2019). These reviews rely on observational data from the field, in situ, and laboratory experiments that are characterized by taxonomic and geographic biases. These biases lead to a lack of understanding of the drivers of isoprene emissions, such as water availability, solar radiation, plant biomass, and temperature, and their combined effects at large spatio-temporal scales.

Trends in drivers of isoprene emissions have been recorded over the last decades. At the global scale, land surface air temperature has increased by 1.41 °C over the period 1880–2018, and over the last 20–30 years photosynthetic activity has risen by 22%–33%, albeit with some spatial variability (Jia et al., 2019). Other drivers of BVOC emissions show high levels of spatio-temporal variability, such as precipitation and soil moisture (Dai, 2013; Hartmann et al., 2003), frequency and intensity of extreme weather events (heatwaves and droughts) (Jia et al., 2019), and the switch in surface solar radiation from “global dimming” (1950–1980) to “global brightening” (after the 1990s) (Hartmann et al., 2003) in response to changes in regional aerosol loads (Wild, 2009, 2012; Streets et al., 2009). These trends may influence isoprene emissions and consequently affect air quality and climate.

To probe trends in isoprene emissions and possible links with trends in isoprene drivers, space retrievals of formaldehyde concentrations provide a powerful, globally homogeneous surrogate. Formaldehyde is an intermediate by-product of the oxidation of volatile organic compounds (VOCs), where oxidation of methane by the hydroxyl radical represents the dominant source (60%) of HCHO, followed by oxidation of biogenic (30%), anthropogenic (7%) and pyrogenic (3%) VOCs (Stavrakou et al., 2009). While methane contributes to the background HCHO abundances, major variations in boundary layer HCHO are driven by isoprene, due to its high molar yield and rapid production of HCHO. This contribution can reach up to 85% during the growing season (Franco et al., 2016) at a spatial scale of ca. 10–100 km (Palmer et al., 2003). Curci et al. (2010) showed that oxidation of monoterpenes contributes very little to HCHO column concentrations across Europe. Hence, estimates of biogenic monoterpene concentrations are not inferred by inversion methods, because sources of isoprene and monoterpenes often co-occur in forested regions and HCHO formation from monoterpenes is small compared to that from isoprene. Thus, retrieval of HCHO column concentrations from remote sensing UV/Vis solar backscatter instruments provides a proxy for local emissions of isoprene, but is not used for terpenes.

Studies have reported trends in formaldehyde column concentrations and their drivers (De Smedt et al., 2010, 2015; Stavrakou et al., 2018), e.g. for specific regions, such as the United States (Zhu et al., 2017), and using model-derived isoprene emissions (Stavrakou et al., 2014; Bauwens et al., 2016; Chen et al., 2018; Yáñez-Serrano et al., 2020; Wang et al., 2021; Opacka et al., 2021). These studies highlighted the main role of temperature and radiation in driving trends in HCHO concentrations and isoprene emissions. To explore the role of water availability and by assuming that ∼ 70–90% of isoprene production is directly linked to photosynthesis, Zheng et al. (2015) analyzed the covariance in global HCHO column concentrations and gross primary productivity (GPP) with meteorological drivers (surface temperature, downward shortwave radiation, photosynthetically active radiation, precipitation) to evaluate isoprene emissions produced by the global Earth system model NASA ModelE2-YIBs (The Yale Interactive Terrestrial Biosphere model). The authors applied different isoprene algorithms, some of which included soil moisture dependence. When soil moisture dependence was accounted for, Zheng et al. (2015) found a positive correlation between isoprene emissions and photosynthesis and a negative correlation between isoprene emissions and HCHO variability, with the opposite occurring when soil moisture dependence was neglected. Zheng et al. (2015) thus suggested the important role of water availability on the intra-seasonal to interannual timescales that needs to be further explored. However, among different drivers, they could only consider precipitation from reanalyses to describe water availability. Here we expand on previous analyses by : (i) investigating the spatial and temporal variability of trends in drivers and HCHO concentrations, (ii) accounting simultaneously for multiple drivers (temperature, water availability, biomass, radiation), and (iii) including diverse drivers that describe water availability (i.e., precipitation, soil moisture, and a drought index).

Based on remotely-sensed HCHO column concentrations, we investigate the relationship between global isoprene emissions and associated global change drivers over the period 2005–2016. We use observations of plant biomass to account for indirect effects of changes in GPP on isoprene emissions (Unger et al., 2013; Zheng et al., 2015), and we apply observations of the aerosol layer and burned fraction to account for anthropogenic and pyrogenic sources of formaldehyde (Stavrakou et al., 2018) and provide a proxy for diffuse radiation (Strada and Unger, 2016; Unger et al., 2017). We ultimately aim to quantify trends in remotely-sensed HCHO column concentrations and the effects of environmental global change drivers, their spatial variability and their interactions with HCHO column concentrations. In particular, we aim to assess whether trends in HCHO concentrations are sensitive to variations in water availability, and whether the sign of this relationship changes across different regions of the world.

## 2. Data and methodology

### 2.1. Observational data-sets

For the analysis period 2005–2016, we use global observation datasets of HCHO column concentrations and environmental drivers,

**Table 1**
Summary of observational data-sets used in the present study.

| Dataset (version) | Variable | Units | Spatial res. | Period | Reference |
|---|---|---|---|---|---|
| Ozone Monitoring Instrument (OMI-L3 vQA4ECV) | Formaldehyde (HCHO) column concentrations | $10^{15}$ molec $cm^{-2}$ | 0.25° | 2005–2017 | De Smedt et al., 2018 |
| Climatic Research Unit gridded Time Series (CRU-TS v4.03) | Mean Surf. Air Temperature | Celsius | 0.50° | 1901–2018 | Univ. East Anglia CRU Harris et al., 2020 |
| | Mean Precipitation Rate | mm $month^{-1}$ | 0.50° | 1901–2018 | Univ. East Anglia CRU Harris et al., 2020 |
| Global Land Evaporation Amsterdam Model (GLEAM v3.3b) | Root-Zone Soil Moisture (RZSM) | $m^3$ $m^{-3}$ | 0.50° | 2003–2017 | Martens et al., 2017 |
| Standardized Precipitation–Evapotranspiration Index (SPEI v2.6) | SPEI | unitless | 0.50° | 1901–2018 | Vicente-Serrano et al., 2010 |
| Copernicus Global Land Service 1-km Version 2 | Leaf Area Index (LAI) | $m^2$ $m^{-2}$ | 0.50° | 2005–2017 | Verger et al., 2019 |
| Moderate Resolution Imaging Spectroradiometer (MODIS) Terra and Aqua monthly mean (C6.1-M3) | Aerosol Optical Depth (AOD) | unitless | 1.0° | 2003–2019 | Levy et al., 2013 |
| Global Fire Emissions Database (GFED v4.1s) | Burned Fraction (BF) | fraction of grid cell | 0.25° | 2003–2016 | Giglio et al., 2013 |

comprising surface air temperature, precipitation, root-zone soil moisture, the Standardized Precipitation–Evapotranspiration Index (SPEI), the Leaf Area Index (LAI) as an indicator of biomass and plant productivity, the burned fraction (BF) as an indicator of fire activity and pyrogenic sources of HCHO, and the aerosol optical depth (AOD) as a proxy for radiation and pyrogenic sources of HCHO ( Table 1).

### *2.1.1. Formaldehyde column concentrations*

We use gridded, Level 3 (L3), monthly mean retrievals of HCHO tropospheric column concentrations provided by the Ozone Monitoring Instrument (OMI) for the period 2005–2016 at a resolution of 0.25° (http://www.qa4ecv.eu; De Smedt et al., 2015. The OMI instrument is a nadir-viewing imaging spectrometer that measures solar radiation backscattered by the Earth's atmosphere and surface in the UV–Vis wavelength range (270-–500 nm) (Levelt et al., 2006). It provides near daily global coverage (De Smedt et al., 2015) due to its Sun-synchronous polar orbit that crosses the Equator around 13:30 Local Time (in ascending mode).

Retrieval of OMI HCHO tropospheric columns relies on an improved differential optical absorption spectroscopy (DOAS) algorithm to derive a top-down constraint of HCHO (De Smedt et al., 2018). This technique derives the column abundance of a trace gas using measurements of electromagnetic radiation in a given spectral interval, whereas a-priori profiles are obtained from a chemistry-transport model (Brasseur and Jacob, 2017). Observations with cloud fractions $>$ 40% are filtered out. While no explicit correction is applied for aerosols, the cloud correction accounts for a large proportion of the aerosol scattering effect (De Smedt et al., 2015). The OMI pixel random uncertainty is of the order of $0.8 \times 10^{16}$ molec $cm^{-2}$ and the systematic error remaining for monthly and regionally averaged columns is about 20%–40% (Stavrakou et al., 2018). Further details on OMI HCHO retrievals and the DOAS algorithm are described in De Smedt et al. (2015, 2018) and Stavrakou et al. (2018). Hereafter, OMI HCHO column concentrations are referred to as HCHO columns.

### *2.1.2. Surface air temperature and precipitation*

We use gridded monthly means (1901–2018) of global (except Antarctica) surface air temperature and precipitation at a resolution of 0.5° from the Climatic Research Unit gridded Time Series (CRU-TS v4.03, https://sites.uea.ac.uk/cru/data/; Harris et al., 2020).

### *2.1.3. Root-zone soil moisture*

Global (50° $N$ to 50° S) gridded monthly mean estimates of root-zone soil moisture (2003–2017) at 0.25° spatial resolution are derived from the Global Land Evaporation Amsterdam Model (GLEAM v3.3b, https://www.gleam.eu/). This uses satellite observations of precipitation and soil moisture assimilated from passive and active C- and L-band microwave sensors of the European Space Agency Climate Change Initiative (Dorigo et al., 2017), plus static data for soil properties, rainfall climatology, and land cover (Martens et al., 2016, 2017). In each grid cell, land cover types influence the number of soil layers and the depth of the root-zone. Hereafter, we refer to root-zone soil moisture as soil moisture.

### *2.1.4. The standardized precipitation-evapotranspiration index*

The SPEI is a multiscalar, standardized drought index that defines monthly anomalies in a climatic water balance over the preceding n months, based on the chosen time-scale (Vicente-Serrano et al., 2010; Beguería et al., 2014). A negative SPEI indicates dryness, while a positive SPEI indicates wetness. SPEI values (1901–2018) are gridded across the global land surface (except areas of desert and ice) to a spatial resolution of 0.5°, and we use a 1-month time scale (SPEI-1 v2.6, https://spei.csic.es/spei_database).

The SPEI is derived using monthly mean temperatures to first calculate monthly potential evapotranspiration (PET). The difference between monthly mean precipitation and PET provides a measure of water balance (surplus or deficit), on which the computation of SPEI is based. The measures of water balance are then aggregated and the resulting cumulative probabilities of water balance are normalized, so that the SPEI has an average value of 0 and a standard deviation of 1.

### *2.1.5. Leaf area index*

We use the Copernicus Global Land Service 1 km version 2 LAI product derived from SPOT/VEGETATION and PROBA-V data for the period from 1999 to May 2014, and from May 2014 to June 2020, respectively, at 1/112° spatial resolution and 10-day frequency (https://land.copernicus.eu/global/products/lai). Neural networks are first trained to retrieve LAI from daily synthesis top of canopy reflectances in the red, near infrared and short wave infrared. Dedicated filtering, smoothing and gap filling techniques are then applied to ensure consistency and continuity of the LAI time course every 10 days using algorithms described by Verger et al. (2014, 2019) and quality assessment criteria described by Sánchez and Camacho (2017) and Fuster et al. (2020).

### *2.1.6. Aerosol optical depth*

Aerosol optical depth is a dimensionless measure of the integrated columnar aerosol load and, as a consequence, of atmospheric transparency, where high AOD indicates low transparency. Since 2002, the Moderate Resolution Imaging Spectroradiometer (MODIS) aboard the Aqua and Terra satellites provides AOD at 550-nm wavelength, indicating where aerosols interfere with photosynthetically active radiation, with different daytime overpass: Terra at 10:30 h and Aqua at 13:30 h. We use the Quality Assured MODIS Collection 6.1 (C6.1) Dark Target Deep Blue Combined monthly mean product (L3) from the NASA Goddard Space Flight Center and the Atmosphere Archive and Distribution System Distributed Active Archive Center (DAAC) (https://ladsweb.modaps.eosdis.nasa.gov/). This is a globally gridded dataset at 1° resolution covering dark and bright surfaces (MODIS L3 C6.1 AOD) (Levy et al., 2010; Shi et al., 2014) and includes significant adjustments compared with previous collections, such as an updated cloud mask to retrieve heavy smoke, an improved quality assurance, and a spatially refined aerosol type map (Levy et al., 2013). For each month, we compute the arithmetic mean between the Terra (MOD08-M3) and Aqua (MYD08-M3) products.

### 2.1.7. Burned fraction

We use global monthly burned fractions at a spatial resolution of 0.25° (1995–2016) from the Global Fire Emissions Database (GFED4) (https://www.globalfiredata.org/; Giglio et al., 2013), where, starting from 2000, the GFED4 monthly burned fraction is derived from the 500-m direct broadcast burned area produced by MODIS Collection 5.1 (MCD64A1 product). We use GFED v4.1s data (Randerson et al., 2012) that combines 1-km thermal anomalies observed outside the burned area maps (active fires) with the 500-m MODIS burned area, thus including small fires that are not detected by the standard GFED4 product.

## 2.2. Statistical analyses

To perform statistical analyses, we aggregate monthly values to annual means and the data are firstly remapped onto a common 1° spatial resolution grid using a distance-weighted remapping function, and then spatially aggregated to a resolution of 2° to reduce spatial autocorrelation and computing requirements.

### 2.2.1. Global and regional temporal trends of formaldehyde columns

To determine temporal changes in HCHO across the study period, we calculate annual Theil–Sen's slopes in OMI HCHO at each grid-cell, using the Theil–Sen slope estimator in the `mblm` package (Komsta, 2012) of the R statistical software (R. Core Team, 2017) that provides a median of all slopes between paired values. This method minimizes the influence of outliers in the calculation of trends as it is more robust to outliers than linear models fitted by ordinary least squares (Stokland et al., 2003; Ohlson and Kim, 2015). We calculate percentage Theil–Sen's slopes with respect to a reference year (at $p < 0.01$) by dividing the Theil–Sen's slopes over 2005–2016 period at each pixel by the 2005 HCHO annual concentration (De Smedt et al., 2010).

### 2.2.2. Drivers of formaldehyde columns

The temporal contributions and the effects of the interactions among drivers on the trends in HCHO columns are analyzed using generalized linear mixed-effects models (GLMMs). These models include a temporal autocorrelation structure for lag 1 (AR1), which stands for temporal autocorrelation with the previous year in our calculation. We apply a random intercept model with pixel (or grid-cell) as the random factor, thus grouping all data belonging to the same pixel. In the model, the OMI HCHO is the response variable and the predictors comprise surface air temperature, precipitation, root-zone soil moisture, SPEI, LAI, AOD, burned fraction, and their first-order interactions at $p < 0.01$ and $p < 0.05$ for global and regional scales, respectively. All model residuals meet the assumptions of normality and heteroscedasticity, and the covariation between predictors do not indicate multicollinearity (i.e., variance inflation factor, VIF$\ll$ 10). The fitting quality of the derived models is assessed via the `r.squaredGLMM` package in R which provides both the marginal and conditional R2 coefficient of a fixed GLMM.

Relationships between predictors and OMI HCHO columns related to temporal variability. Variations in driver effects on trends in OMI HCHO are tested using the `TempCont` package in R (Fernández-Martínez et al., 2017; Fernández-Martínez et al., 2019), which uses GLMMs to disentangle the effect of one single predictor, while taking into account the variance (or correlation) shared with other predictors. Then, `TempCont` calculates and compares temporal trends predicted by the GLMM for the selected predictor when it is held constant and when it is allowed to vary. The difference between these temporal predictions is the average temporal contribution of that predictor to the trend in OMI HCHO, and the difference between all individual temporal contributions and the observed trend represents unknown contributions. `TempCont` also calculates the average sensitivity of the response variable to predictor changes by dividing the temporal contributions by the trends of the predictor variables. All errors are calculated using the error-propagation method.

GLMMs account for first-order interactions between predictors, therefore we apply the visreg package in R which simultaneously visualizes the effects of spatial variability in two explanatory variables on the spatial trends in OMI HCHO. Using statistically significant first-order interactions between predictors contributing to the final GLMMs, we produce cross-sectional plots that illustrate a 1-D relationship between OMI HCHO and a single predictor (continuous term) by taking cross sections at the 10th and 90th percentiles of another predictor (fixed term). Since GLMMs and interactions accounted in the models do not always involve the same statistically significant predictors, we compare cross-sectional plots that involve the same or related (e.g., for water availability) predictors over different regions. We apply the TempCont method to investigate the effect of trends in predictors on trends in temporal variability in OMI HCHO columns, while we show the spatial relationships using partial residual plots provided by the visreg R package.

# 3. Results

## 3.1. Global and regional trends in formaldehyde columns

Annual average HCHO columns for the study period (2005–2016) are higher over the south-east United States, Central America, the Amazon Basin, central and southern Africa, India, south-east China, Southeast Asia, and northern Australia (8–14 × $10^{15}$ molec cm$^{-2}$ yr$^{-1}$) than across southern Australia and Europe (4–10 × $10^{15}$ molec cm$^{-2}$ yr$^{-1}$) (Fig. 1).

While there are no clear global trends in HCHO columns (median: $0.0023\,\sigma$ yr$^{-1}$, mean: $-0.0015\pm0.0014\,\sigma$ yr$^{-1}$; Fig. 2.a), there are regional decreases where HCHO columns are high (Fig. 2.b–c). For example, decreases in HCHO columns between 2005 and 2016 are detected over central Europe and southern Africa (absolute change: −2.0 to $-1.0\times10^{15}$ molec cm$^{-2}$ yr$^{-1}$; proportional change: −2 to −1% yr$^{-1}$), central-west and north-west Amazon Basin (absolute change: −3.0 to 1.5 × $10^{15}$ molec cm$^{-2}$ yr$^{-1}$, respectively; proportional change: −2 to 2% yr$^{-1}$); and southern Australia (absolute change: −2.5 to −1.0 × $10^{15}$ molec cm$^{-2}$ yr$^{-1}$, proportional change: −4 to −1% yr$^{-1}$). In contrast, HCHO columns increase over India, China and the Southeast Asian mainland (absolute change: 1.0 to 2.5 × $10^{15}$ molec cm$^{-2}$ yr$^{-1}$; proportional change: 1 to 3% yr$^{-1}$).

### 3.1.1. Spatial relationship between formaldehyde and its drivers

At the global and some regional scales (Amazon, Australia, Europe, and India-China), cross sectional plots show that spatial variability in HCHO columns positively correlates with the spatial variability in temperature (Fig. 3); however, the effect of local average precipitation and soil moisture modifies this relationship across regions. At the global scale and across India-China, the positive relation between HCHO columns and temperature intensifies (steeper slope) in areas with low precipitation (Figs. 3a and 3b), while over the Amazon Basin the relation changes direction, from positive to negative, where local mean precipitation shifts from low to high (Fig. 3.c) and where local mean soil moisture is low (Fig. 3.d). In contrast, at the global scale, there is no dependence of HCHO columns on temperature where soil moisture is low (Fig. 3e).

Water availability modulates HCHO columns globally and across some regions (Fig. 4). At the global scale, and over the Amazon Basin and India–China regions, the HCHO columns are negatively correlated with precipitation, with behaviors that differ based on soil moisture. At the global scale this relation is stronger where mean soil moisture is high (Fig. 4.a), while over the Amazon Basin region the HCHO–precipitation correlation is more negative (i.e., steeper slope) at low soil moisture levels (Fig. 4.b). Across India and China, the negative relation between HCHO columns and precipitation under high levels

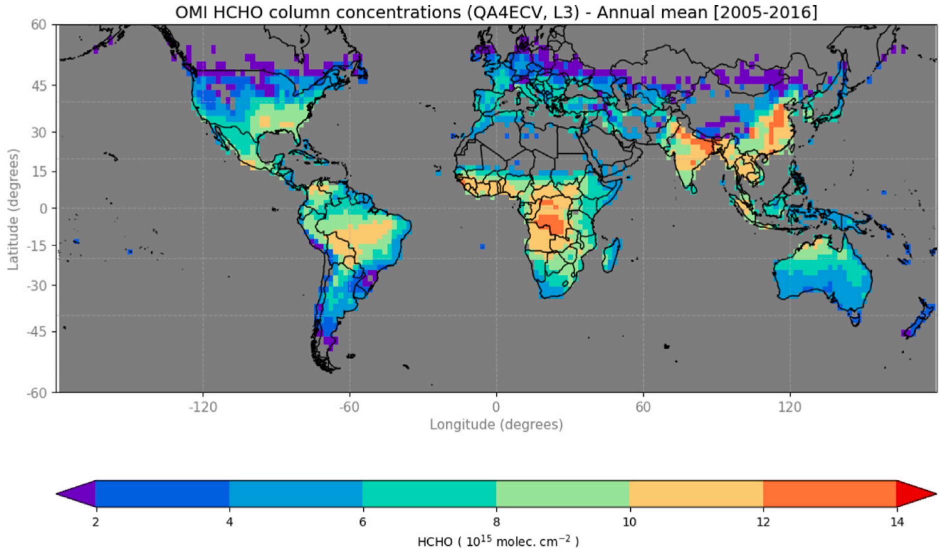

**Fig. 1.** Spatial distribution of annual mean of formaldehyde column concentrations provided by the Ozone Monitoring Instrument (OMI) over 2005–2016 (horizontal res.: 2° × 2°).

of soil moisture becomes positive when soil moisture is low (Fig. 4.c). In contrast, across Australia there is a positive correlation between HCHO columns and precipitation that increases under low levels of soil moisture (Fig. 4.d).

Concentrations of HCHO are driven by the interaction between water availability and plant biomass (Fig. 5). At the global scale, over the Amazon Basin, India–China and Europe regions, low soil moisture anomalies are associated with high HCHO columns where mean LAI values are high (Figs. 5.a–d).

### 3.1.2. Temporal contribution of trends in drivers to trends in formaldehyde columns

Based on GLMMs, the observed trends in HCHO columns show declines at the global scale ($-0.02 \pm 0.01 \times 10^{15}$ molec $cm^{-2}$ $decade^{-1}$) and across the Amazon Basin ($-0.38 \pm 0.05 \times 10^{15}$ molec $cm^{-2}$ $decade^{-1}$), Australia ($-0.70 \pm 0.03 \times 10^{15}$ molec $cm^{-2}$ $decade^{-1}$), and Europe ($-0.24 \pm 0.05 \times 10^{15}$ molec $cm^{-2}$ $decade^{-1}$), and increments across the India-China region ($0.67 \pm 0.03 \times 10^{15}$ molec $cm^{-2}$ $decade^{-1}$) ( Table 2 and Fig. 6). Over the Amazon Basin region, despite very few pixels show statistically significant trends via the Theil Sen's estimator (Fig. 2), the region consistently presents a decrease in HCHO columns over time via the GLMMs (Table 2). Trends in HCHO columns derived from the GLMMs (Table 2) agree on sign, while differ in magnitude and in statistical significance, with trends estimated via the Theil–Sen's estimator (Fig. 2) since the GLMM approach pools together many pixels at the same time, thus providing an average slope over all pixels.

In term of drivers, there are positive temporal trends in temperature anomalies at both global and regional scales and contrasting trends in drivers of water availability, such as precipitation, soil moisture, and SPEI (Table 2). Variabilities in annual precipitation, soil moisture, and SPEI are similar across regions (Fig. S.1). We also find increases in LAI at global and regional scales (Table 2), decreases in AOD across China and increases in AOD across India (Fig. S.2), and a negative trend in burned fraction in all regions, except for India-China (Table 2).

Impacts of drivers of HCHO columns vary between regions ( Table 2). At the global scale and across the Amazon Basin and India-China regions, positive trends in temperature yield increases in HCHO columns, except over Australia where this relation is negative.

Trends in drivers related to water availability (precipitation, soil moisture, and SPEI) have a different temporal contribution to trends in HCHO columns (Fig. 6), with declining precipitation mostly associated with declining HCHO columns, while increasing soil moisture and negative trends in SPEI tend to enhance HCHO columns (Table 2). However, there are regional differences in these effects. Across Europe, a negative trend in SPEI (drier conditions) is associated with increases in HCHO, while over the Amazon Basin it is the negative trend in soil moisture that has a positive temporal contribution to trends in HCHO columns; over these two regions, positive temporal contributions of water stress counteract the overall observed negative trend in HCHO (Figs. 6.b-d).

We find that LAI, AOD, and BF are associated with trends in HCHO, albeit with different directions (Table 2). Temporal increases in LAI are associated with reduced HCHO columns at the global scale and across Australia, while the opposite occurs across India-China. In India-China the negative trends in AOD are positively related with trends in HCHO, while the opposite is found at the global scale and over the Amazon Basin region and Europe, where decreases in AOD lead to decreases in HCHO. Decreases in BF are associated with declining HCHO at the global scale and across the Amazon Basin region and Europe, while across India-China positive trends in BF are associated with increases in HCHO, although these relationships are not statistically significant.

Overall, our statistical models reproduce the observed inter-annual variability in HCHO columns as well as the sign of the regional temporal trends. In general, based on the estimated conditional $R^2$ of the fixed models, the GLMMs explain > 90% of the global variation in HCHO columns, 70%–80% of which is explained by our predictors (marginal R2), with the remaining 20%–30% related to variability among pixels. Over the Amazon Basin, Europe and India–China regions, the GLMMs explain at least 33% of the variation in HCHO columns, while over Australia the GLMMs present substantial unknown contributions, suggesting that the results should be interpreted with caution over this region (Fig. 6).

## 4. Discussion

### 4.1. Regional trends in formaldehyde columns

The magnitudes and directions of regional annual trends in HCHO columns identified by our analysis based on the Theil–Sen's estimator are similar to those described by De Smedt et al. (2010), based on HCHO retrieved by GOME/ERS-2 and SCIAMACHY/ENVISAT (1997–2009). The authors reported annual increases in HCHO over China ($0.8 \pm 0.2 \times 10^{14}$ molec $cm^{-2}$ $yr^{-1}$; $3 \pm 0.8\%$ $yr^{-1}$) and maximum over Beijing–Tianjin–Hebei ($4 \pm 1.4\%$ $yr^{-1}$) and northern China (between $6.4 \pm 2.8\%$ $yr^{-1}$ and $9.7 \pm 4.1\%$ $yr^{-1}$), with homogeneous increases across India ($1.1 \pm 0.2 \times 10^{14}$ molec $cm^{-2}$ $yr^{-1}$; $1.6 \pm 0.4$ $yr^{-1}$). De Smedt et al. (2010)

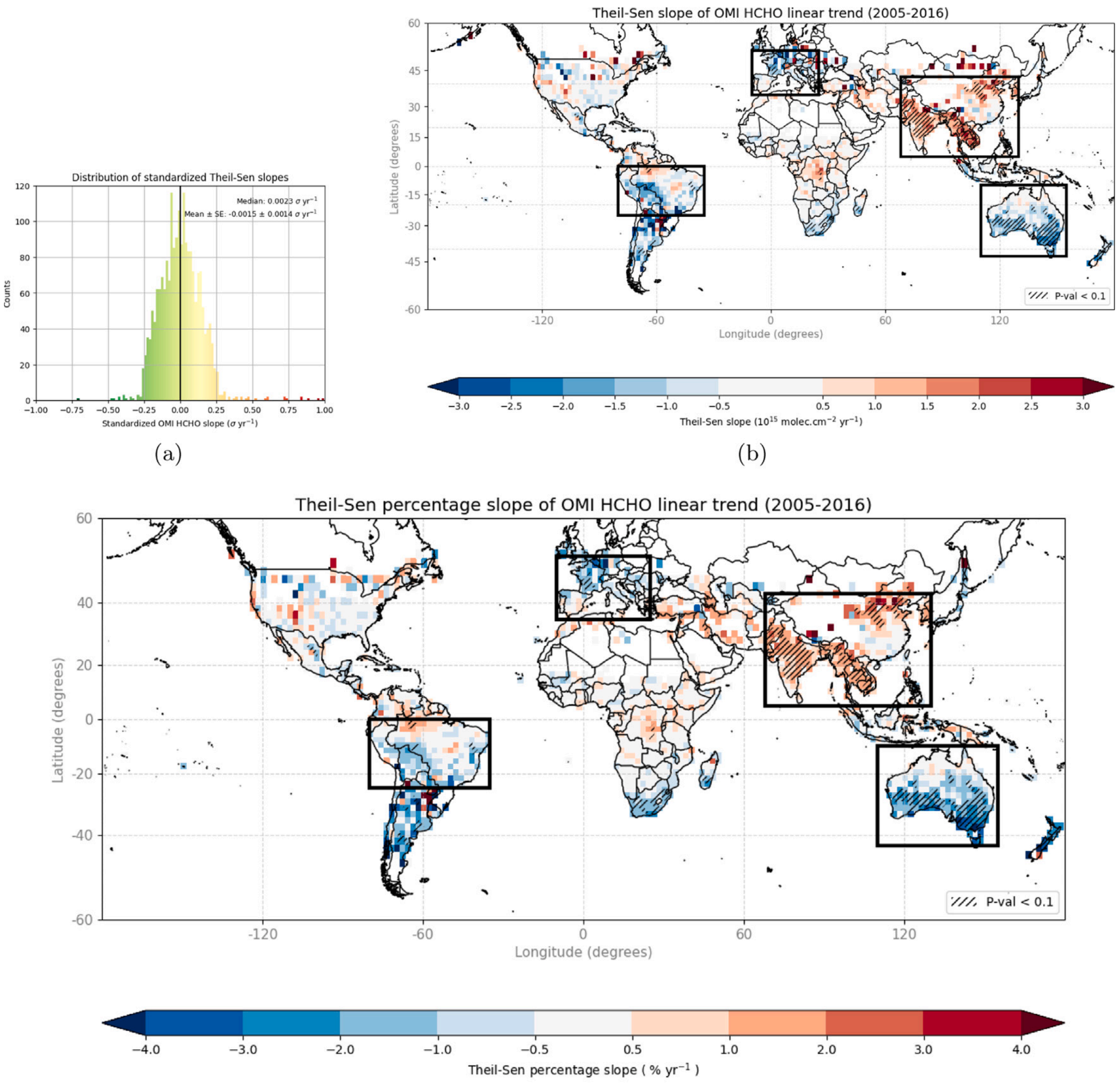

(a)

(b)

(c)

**Fig. 2.** Spatial distribution of Theil–Sen's slopes of HCHO annual column concentrations calculated over 2005–2016: (a) distribution of standardized slopes (units: $\sigma$ yr$^{-1}$)), (b) absolute slopes (units: $10^{15}$ molec cm$^{-2}$ yr$^{-1}$), and (c) percentage slopes (units: % yr$^{-1}$). At each pixel, percentage slopes are calculated by dividing Theil–Sen's slopes over 2005–2016 by the corresponding HCHO annual columns for 2005 (reference year). Hatched regions indicated areas where Theil–Sen's slopes are significant at the 90% confidence level ($p$-value $< 0.1$). Black boxes highlight areas selected for regional analysis: Amazon [25°S–0°; 35°–80°W]; Australia [10°–43°S; 110°–155°E]; Europe [35°–52°N; 10°W–25°E]; and India–China [5°–42.5°N; 68°–130° E].

attributed these positive trends to regional increases in anthropogenic emissions from combustion of fossil fuels and other industrial processes. Emissions of anthropogenic VOCs dominate across India and China, while emissions of biogenic VOCs are located over northern India and southern China, and pyrogenic VOCs are produced by agricultural fires in the North China Plain Stavrakou et al. (2016). Based on temperature-corrected OMI HCHO data over 2005–2019 in Asia, Bauwens et al. (2022) reported significant trends over large cities, either positive (due to the absence or limited efforts to regulate anthropogenic VOC precursors of HCHO) or negative (due to the implementation of efficient abatement measures). Recent studies of the effects of land cover have linked increases in isoprene emissions and HCHO columns to afforestation in India, north-east and southern China (Chen et al., 2018; Wang et al., 2021) and areas with high levels of vegetation cover across northeast, central, and southern China (Wang et al., 2021). Exploration of trends in the OMI HCHO columns (November 2004 to August 2014) by De Smedt et al. (2015) showed increases across India and China and decreases across North America and Europe, due to emission controls, and across South America, particularly over the Brazilian state of Rondônia, due to a decline in deforestation rates between 2005 and 2010.

Our analysis shows trends in HCHO columns over the contiguous United States and southern Canada (Fig. 2) similar to those reported by Zhu et al. (2017) for the periods 2005–2009 to 2010–2014, including decreases across the south-eastern United States (due to decreases in anthropogenic VOC emissions) and increases elsewhere (probably related to regional afforestation).

The observed trends in HCHO columns across most regions match those in OMI-based isoprene emissions reported in the literature, including Bauwens et al. (2016) who found declines between 2005 and 2013 across the Amazon Basin (−2.1% yr$^{-1}$), U.S. (−3.7% yr$^{-1}$) and western Europe (−3.9% yr$^{-1}$), and Yáñez-Serrano et al. (2020) who found decreases across the Amazon Basin of −1.36% yr$^{-1}$ over 2005–2014. As opposed to our results, however, Bauwens et al. (2016) reported decreases in HCHO columns over south China (−0.7% yr$^{-1}$), which resulted in a negative trend in the OMI-derived isoprene fluxes (−1.6% yr$^{-1}$), likely attributed to the crop expansion and the declining solar radiation in this region (Yue et al., 2015).

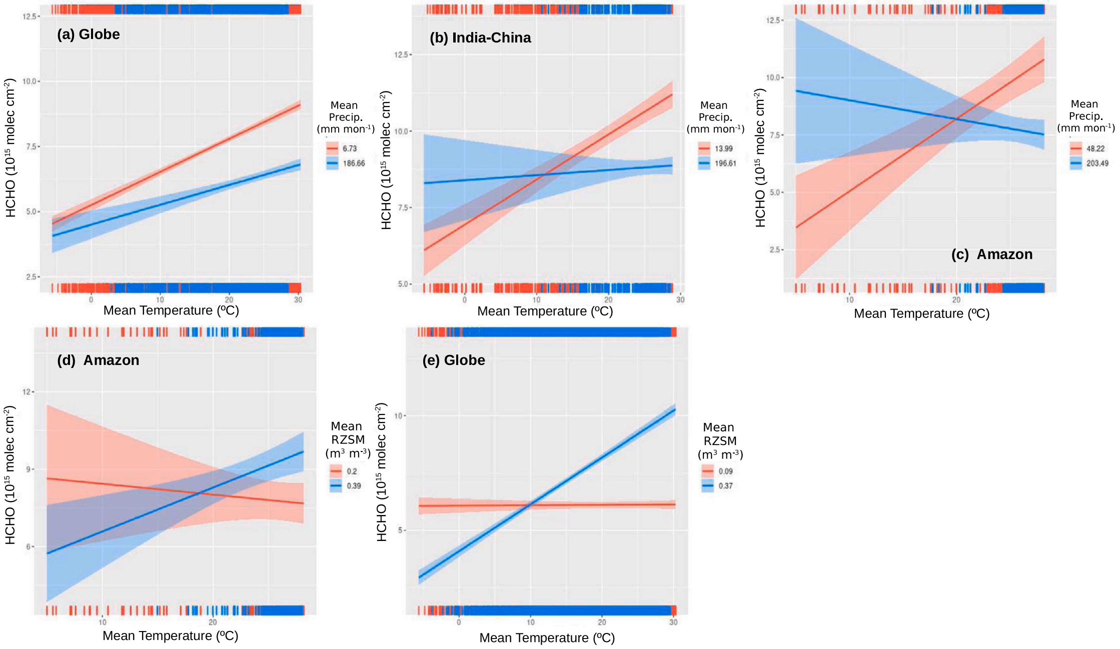

**Fig. 3.** Cross sectional plots depict the effect of the spatial variability in surface air temperature (X-axis) on the spatial variability in HCHO columns (Y-axis) under high (i.e., above the 90th percentile) or low (i.e., below the 10th percentile) local mean precipitation (units: mm month-1), or root-zone soil moisture (units: m3 m−3), where the interaction between temperature (continuous term) and precipitation/soil moisture (constant term) is active in the Generalized Linear Mixed-effects models. The bold line displays the regression line; shaded areas represent the confidence interval; colored ticks at the top and the bottom of each plot display partial residuals of each regression model (positive residuals at the top, negative residuals at the bottom).

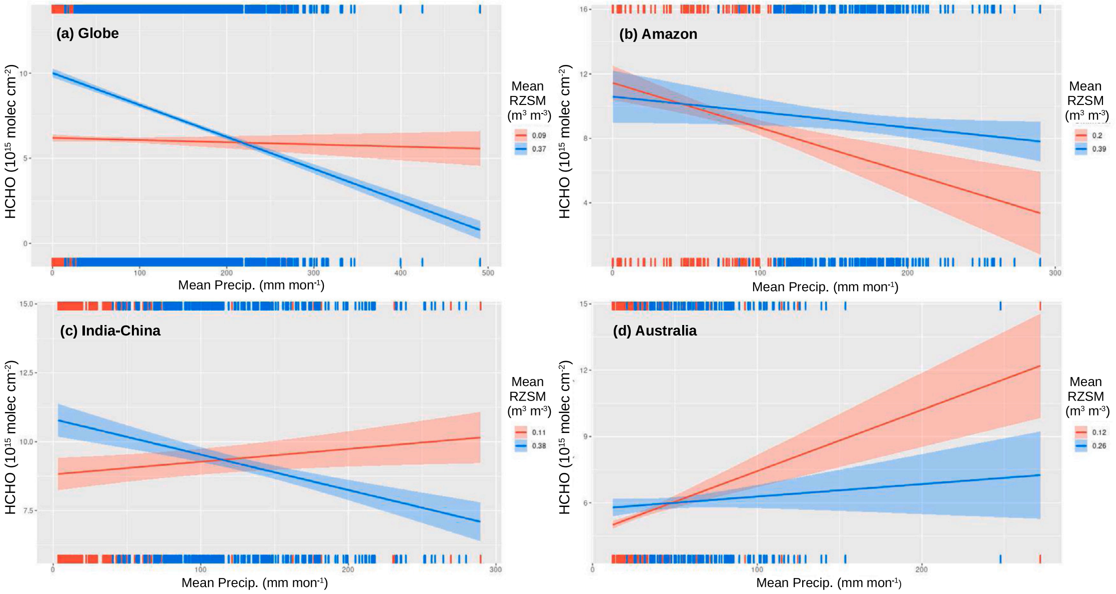

**Fig. 4.** Cross sectional plots depict the effect of the spatial variability in precipitation (X-axis) on the spatial variability of HCHO columns (Y-axis) under high (i.e., above the 90th percentile) or low (i.e., below the 10th percentile) local mean root-zone soil moisture (units: $m^3$ $m^{-3}$), where the interaction between precipitation (continuous term) and root zone soil moisture (constant term) is active in the Generalized Linear Mixed-effects models. The bold line displays the regression line; shaded areas represent the confidence interval; colored ticks at the top and the bottom of each plot display partial residuals of each regression model (positive residuals at the top, negative residuals at the bottom).

### 4.2. *Trends in drivers of formaldehyde columns*

Our analysis shows large temporal variations in HCHO columns and associated drivers (Fig. S.1). At the global scale, and as previously observed for isoprene emissions (Stavrakou et al., 2014; Opacka et al., 2021 and references therein), maxima and minima in HCHO columns correlate with El Niño (2004/2005, 2009/2010 and 2014/2016) and La Niña (2007–2009) episodes, respectively.

Across the Amazon Basin, precipitation, soil moisture, and SPEI related to drought conditions in 2005, 2010, and 2015 (Aragão et al., 2018) are associated with peaks in HCHO columns (Stavrakou et al., 2015; Morfopoulos et al., 2022). Across Australia, increases in temperature during the heatwaves of the summers of 2008–2009 and 2012–2013 and shifts in precipitation, soil moisture, and SPEI from the “Millennium Drought/Big Dry” period of 1995–2009 to the “Big Wet” period of 2010–2012 (Taschetto et al., 2016) do not show a clear impact on HCHO columns. Across Europe, the dry summer of

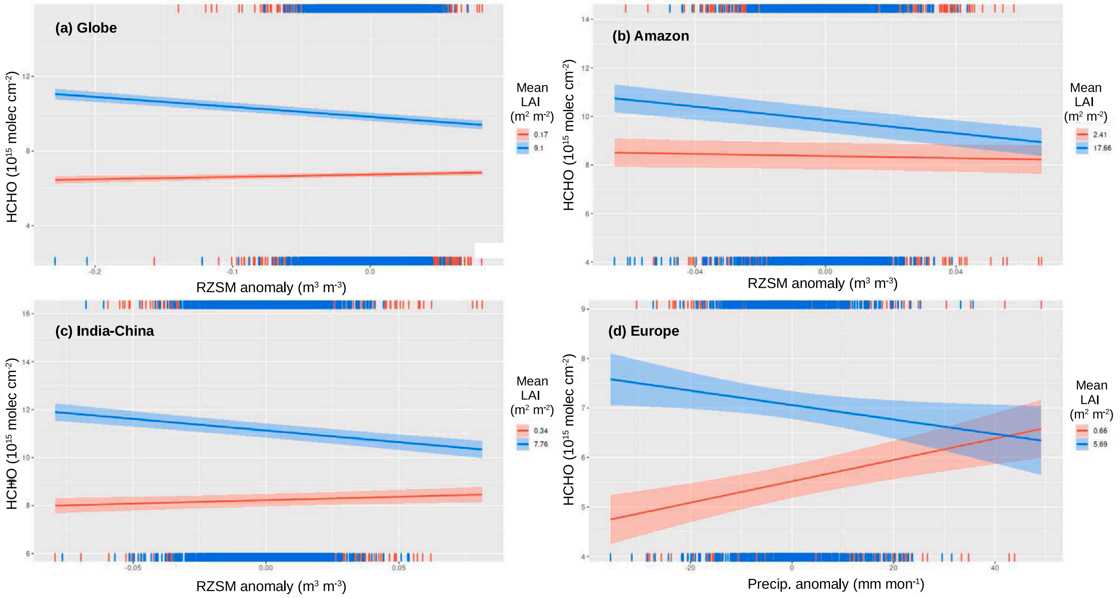

**Fig. 5.** Cross sectional plots depict the effect of the spatial variability in water availability (X-axis; root-zone soil moisture/precipitation) on the spatial variability of HCHO (Y-axis) under high (i.e., above the 90th percentile) or low (i.e., below the 10th percentile) Leaf Area Index (units: $m^2$ $m^{-2}$), where the interaction between root-zone soil moisture/precipitation (continuous term) and LAI (constant term) is active in the Generalized Linear Mixed-effects models. The bold line displays the regression line; shaded areas represent the confidence interval; colored ticks at the top and the bottom of each plot display partial residuals of each regression model (positive residuals at the top, negative residuals at the bottom).

2015 (Orth et al., 2016) leads to a peak in HCHO columns. Across India-China, the "cold period" between 2008 and 2012, which Stavrakou et al. (2014) related to a decrease in isoprene emissions, does not affect HCHO in our study.

Although the combined effects of a short time record (2005–2016) and natural variability on the computed trends may lead to mismatches with long-term climate trends, our analyses reveal statistically significant temporal patterns in drivers of HCHO columns ( Table 2) which support previously reported findings. Among them we find: (i) increases in temperature and LAI (Jia et al., 2019), (ii) decreases in AOD indicating a "global brightening" period (Wild, 2012; Hartmann et al., 2003); (iii) decreases in BF (Jia et al., 2019); (iv) large spatial variability in drivers related to water availability (precipitation, soil moisture and SPEI) (Hartmann et al., 2003). We find annual decreases in water availability indicators across the Amazon Basin region (see predicted trends for the region in precipitation, RZSM and SPEI in Table 2) in agreement with a regional decline in rainfall (Aragão et al., 2018) and reduced vegetation greenness (Hilker et al., 2014) reported in the literature. Across Europe, among water availability indicators, only SPEI shows a negative predicted trend ( Table 2) that indicates increased aridity, which characterized the region since 1950 (Dai, 2013; Hartmann et al., 2003; Vicente-Serrano et al., 2014; Spinoni et al., 2015).

### *4.3. Sensitivity and temporal contribution of drivers on formaldehyde columns*

Trends in temperature, LAI, and AOD are important drivers of trends in HCHO columns ( Table 2). Stavrakou et al. (2014) showed that increasing temperatures led to increment in model-based isoprene emissions across Asia during the period 1979–2012, while at the global scale Zheng et al. (2015) demonstrated a strong positive correlation across seasons (i.e., spring, summer, autumn) over the period 2005–2011. Similarly, we find a positive relationship between spatial variabilities in HCHO columns and in temperature (Fig. 3) and a positive sensitivity across years in HCHO columns to temperature over most regions, except across Australia ( Table 2). Based on the analysis of spatial relationships, water availability influences the HCHO-temperature correlation. For example, over the Amazon Basin, different explanatory variables used to take cross sections of the HCHO-temperature relationship (i.e., precipitation and soil moisture) lead to different correlations (Fig. 3.c vs. Fig. 3.d). Although variables measuring water availability are related, it is important to consider that cross-sectional plots show the relationship of the explanatory variable vs the response variable when the variance of all the other predictors have already been taken into account. So, the interaction temperature–soil moisture has to be understood as once we have removed the effect of precipitation-temperature from the data. In addition, when focusing on HCHO as a proxy of isoprene emissions, there could be a delay between the effect of precipitation and soil moisture on vegetation functioning, with precipitation affecting vegetation processes in the short term, while soil moisture in the long term. Also, precipitation has different consequences than soil moisture (e.g., when it rains, direct radiation decreases while diffuse radiation increases, which may alter some metabolic processes etc.). Compare to other regions, across Australia precipitation and soil moisture play a more important role than temperature (Fig. 4). These results indicate that raising temperatures across Australia, which are often tied to dry conditions, may limit isoprene emissions, as also shown by previous studies (Müller et al., 2008; Sindelarova et al., 2014; Stavrakou et al., 2015; Bauwens et al., 2016; Emmerson et al., 2019).

At the global scale, we find that positive trends in LAI have a negative temporal contribution on the trends in HCHO columns ( Table 2 and Fig. 6), partly in agreement with Opacka et al. (2021) and Chen et al. (2018), who assessed effects of land cover change on global isoprene emissions derived from the BVOC emission model MEGAN2.1 (Model of Emissions of Gases and Aerosols from Nature, Guenther et al., 2012). Opacka et al. (2021) derived isoprene emissions using three different inventories of land cover distribution and reported that land cover change induced a slight negative trend over the period 2001–2016 (between 0.04 and 0.33% $yr^{-1}$), whereas a positive increase in global isoprene emissions (+0.94% $yr^{-1}$) was driven by temperature and solar radiation changes. They further estimated that trends in LAI contributed a small increase (+0.06% $yr^{-1}$) to global isoprene emissions. Over 2000–2015, Chen et al. (2018) estimated that land cover change drove a 1.5% decrease in global isoprene emissions, due

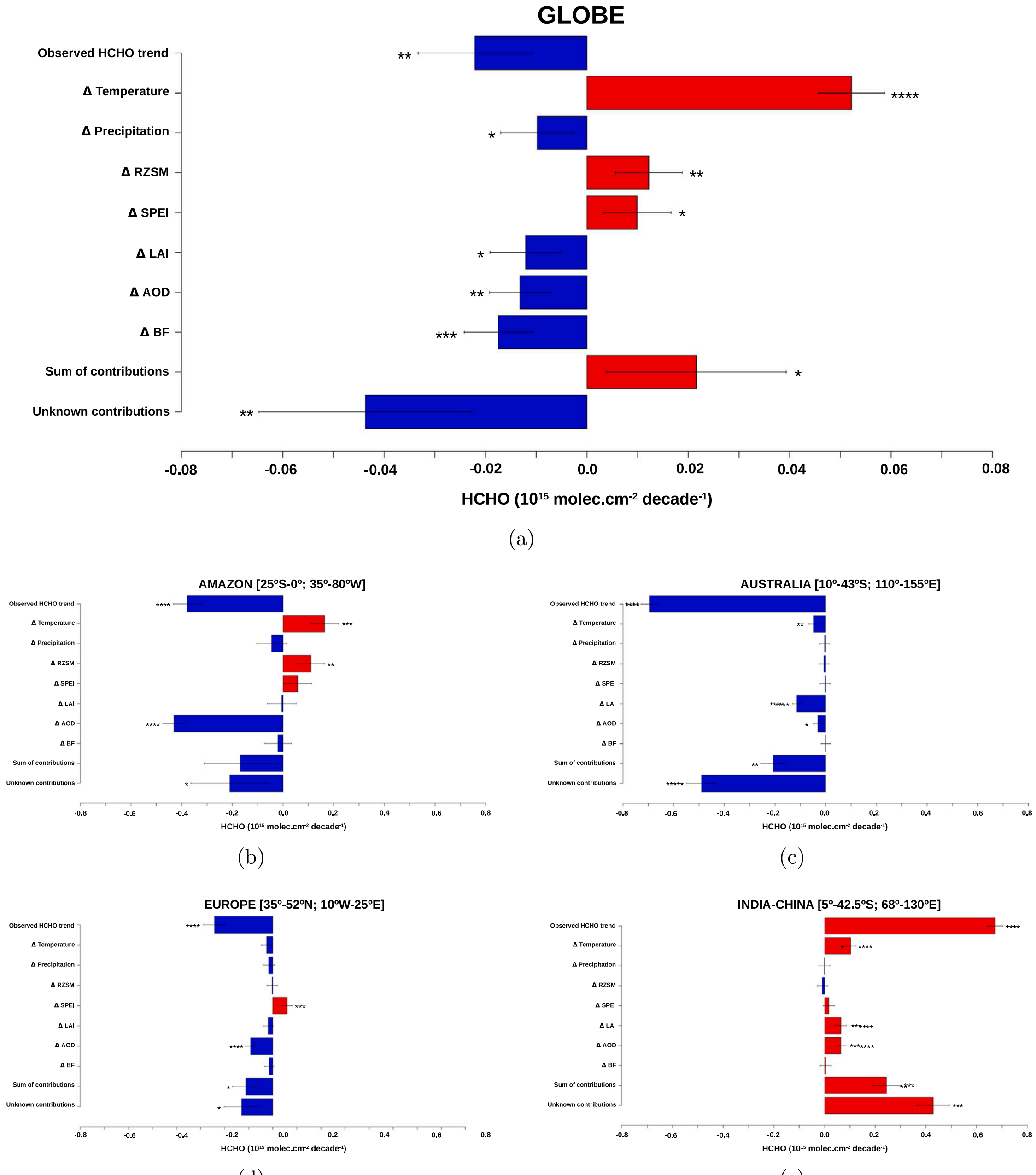

(a)

(b)

(c)

(d)

(e)

**Fig. 6.** Temporal contribution of predictors on HCHO columns (units: $10^{15}$ molec cm$^{-2}$ decade$^{-1}$) over 2005–2016 at the (a) global scale, and over the selected regions: (b) Amazon, (c) Australia, (d) Europe, and (e) India-China (see Fig. 2). Predictors: surface air temperature, precipitation, the Standardized Precipitation-Evapotranspiration Index (SPEI), root-zone soil moisture (RZSM), Leaf Area Index (LAI), Aerosol Optical Depth (AOD) and burned fraction (BF). The difference between all individual temporal contributions and the observed trend represents unknown contributions to the temporal variation in HCHO columns. Error bars indicate standard errors. Significance levels: (*) $p$-value $< 0.1$; (**) $p$-value $< 0.05$; (***) $p$-value $< 0.01$; (****) $p$-value $< 0.001$. See Table 2 for related statistics.

to a combined increase in needle-leaf trees and a decrease in broad-leaf trees and non-tree plants.

At the regional scale, we find that increments in LAI lead to increases in HCHO columns across India-China ( Table 2), supporting estimates by Chen et al. (2018) and Wang et al. (2021) who linked positive trends in HCHO to afforestation programme in the region. Over the other regions, we find that increases in LAI lead to temporal decreases in HCHO columns. Chen et al. (2018) and Yáñez-Serrano et al. (2020) also reported declines in isoprene emissions over Australia and across the Amazon Basin; however, they attributed these decreases in isoprene emissions to reduction in vegetation cover due to wildfires and deforestation. Moreover, (Chen et al., 2018) documented isoprene emission increases across Europe attributed to afforestation.

Overall, our statistical models support some of the findings reported by Chen et al. (2018), that temporal increases in LAI lead to decreases in HCHO columns at the global scale and to increases in HCHO columns across India-China, with conflicting results for Australia, the Amazon Basin and Europe. These latter differences may be due to discrepancies in temporal trends in LAI and land cover change that exist between available inventories (Opacka et al., 2021) and to the use of different sources to investigate trends in isoprene emissions. For example, Chen et al. (2018) estimated isoprene emissions with MEGAN2.1, while we used HCHO retrievals. Across Australia and the Amazon Basin, the used LAI product does not seem to capture deforestation which may be partially driving a negative trend in OMI HCHO columns over these regions. Across Europe, afforestation from 1850 onward mainly

**Table 2**

Trends in predictor anomalies, their temporal contribution to trends in HCHO concentrations and sensitivity of HCHO columns to trends in predictor anomalies as computed by the Generalized Linear Mixed-Effects Model (GLMM) over the globe and over four selected regions (Fig. 2). Predictors: surface air temperature, precipitation, root-zone soil moisture (RZSM), the Standardized Precipitation-Evapotranspiration Index (SPEI), Leaf Area Index (LAI), Aerosol Optical Depth (AOD) and burned fraction (BF). Temporal contribution is the difference between the temporal prediction for the full GLMM and the temporal prediction of the GLMM when one variable is fixed (robust temporal contributions in bold). Sensitivity of the response variable to a predictor change corresponds to the ratio between the temporal contribution and the trend of the selected predictor. Unknown temporal contribution is the difference between the HCHO observed trend and the addition of all temporal contributions. All numbers are multiplied by 10 and expressed in units of $10^{15}$ molec $cm^{-2}$ $decade^{-1}$. For all terms, standard error and significancy are provided.

| Region | | Temp. | Precip. | RZSM | SPEI | LAI | AOD | BF | HCHO Obs. Trend | Unknown temp. contribution |
|---|---|---|---|---|---|---|---|---|---|---|
| Globe | Temporal contribution | **0.0522 ± 0.0065****** | **−0.0098 ± 0.0072*** | **0.0122 ± 0.0066**** | **0.0099 ± 0.0067*** | **−0.0121 ± 0.0070*** | **−0.0132 ± 0.0061**** | **−0.0175 ± 0.0067***** | **−0.0221 ± 0.0112**** | **−0.0437 ± 0.0210**** |
| | Predictor trend | 0.2374 ± 0.0065**** | −1.6874 ± 0.2251**** | 0.0008 ± 0.0003*** | −0.0228 ± 0.0378 | 0.2170 ± 0.0046**** | −0.0034 ± 0.0006**** | −0.0004 ± 0.0002** | | |
| | Sensitivity | 2.1986 ± 0.2802**** | 0.0581 ± 0.0433* | 156.6172 ± 103.8078* | −4.3440 ± 7.7874 | −0.5558 ± 0.3226* | 39.4701 ± 19.4620** | 394.8692 ± 218.1180** | | |
| Amazon<br>(25°S–0; 35°–80°W) | Temporal contribution | **0.1643 ± 0.0556***** | −0.0451 ± 0.0584 | **0.1106 ± 0.0538**** | 0.0576 ± 0.0554 | −0.0050 ± 0.0570 | **−0.4302 ± 0.0443****** | −0.0203 ± 0.0534 | **−0.3783 ± 0.0540****** | **−0.2101 ± 0.1531*** |
| | Predictor trend | 0.3746 ± 0.0133**** | −10.5183 ± 1.0114**** | −0.0112 ± 0.0009**** | −0.2370 ± 0.0259**** | 0.2292 ± 0.0263**** | −0.0367 ± 0.0023**** | −0.0005 ± 0.0001**** | | |
| | Sensitivity | 4.3858 ± 1.4928*** | 0.0429 ± 0.0556 | −99.1357 ± 48.9780** | −2.4290 ± 2.3546 | −0.2202 ± 2.4857 | 117.1870 ± 14.1122**** | 442.5226 ± 1167.581 | | |
| Australia<br>(10°–43°S; 110°–155°E) | Temporal contribution | **−0.0488 ± 0.0198**** | −0.0044 ± 0.0191 | −0.0066 ± 0.0191 | −0.0025 ± 0.0193 | **−0.1141 ± 0.0174****** | **−0.0305 ± 0.0188*** | 0.0004 ± 0.0186 | **−0.6962 ± 0.0328****** | **−0.4897 ± 0.0597**** |
| | Predictor trend | 0.2255 ± 0.0297**** | 1.7375 ± 0.6354*** | 0.0084 ± 0.0011**** | 0.0601 ± 0.0253** | 0.2988 ± 0.0178**** | −0.0004 ± 0.0006 | −0.0001 ± 0.0003 | | |
| | Sensitivity | −2.1650 ± 0.9218** | −0.0252 ± 0.1101 | −7.8241 ± 22.6058 | −0.4209 ± 3.2099 | −3.8185 ± 0.6243**** | 766.2625 ± 1296.6930 | −60.8567 ± 2659.9080 | | |
| Europe<br>(35°–52°N; 10°W–25°E) | Temporal contribution | −0.0251 ± 0.0214 | −0.0168 ± 0.0232 | −0.0027 ± 0.0211 | **0.0594 ± 0.0209***** | −0.0191 ± 0.0204 | **−0.0920 ± 0.0204****** | −0.0155 ± 0.0197 | **−0.2419 ± 0.0467****** | **−0.1300 ± 0.0726*** |
| | Predicted trend | 0.5294 ± 0.0304**** | 1.4099 ± 0.7741** | 0.0036 ± 0.0014*** | −0.0861 ± 0.0256*** | 0.2412 ± 0.0151**** | −0.0229 ± 0.0010**** | −0.0001 ± 0.0001**** | | |
| | Sensitivity | −0.4748 ± 0.4043 | −0.1195 ± 0.1773 | −7.5126 ± 56.5669 | −6.8994 ± 3.1754** | −0.7936 ± 0.8470 | 40.1689 ± 9.0492**** | 1790.933 ± 2313.611 | | |
| India-China<br>(5°–42.5°N; 68°–130°E) | Temporal contribution | **0.1033 ± 0.0205****** | −0.0009 ± 0.0217 | −0.0088 ± 0.0205 | 0.0167 ± 0.0228 | **0.0647 ± 0.0216***** | **0.0644 ± 0.0202***** | 0.0050 ± 0.0217 | **0.6730 ± 0.0293****** | **0.4286 ± 0.0635***** |
| | Predictor trend | 0.1219 ± 0.0185**** | −0.3974 ± 0.7427 | 0.0065 ± 0.0008**** | 0.0760 ± 0.0152**** | 0.3040 ± 0.0128**** | −0.0079 ± 0.0025*** | 0.0002 ± 0.0001**** | | |
| | Sensitivity | 8.4772 ± 2.1172**** | 0.0216 ± 0.5466 | −13.5197 ± 31.6842 | 2.1833 ± 3.0328 | 3.1277 ± 0.7157*** | −81.6750 ± 36.7535** | 273.6728 ± 1183.0830 | | |

*Significance level: $p$-value $< 0.1$.

**Significance level: $p$-value $< 0.05$.

***Significance level: $p$-value $< 0.01$.

****Significance level: $p$-value $< 0.001$.

converted broad-leaved forests into needle-leaved forests, with an increase in needle-leaved (+633000 km$^2$) at the expense of broadleaved forests (−436000 km$^2$) (Bürgi and Schuler, 2003). Since needle-leaved trees mainly emit monoterpenes while broadleaf trees mainly emit isoprene, this conversion in tree species may have led to an increase in monoterpenes emissions, which are not sensed by HCHO retrievals, along with a decrease in isoprene emissions, thus potentially explaining our results.

The type of vegetation cover also influences the spatial relationship between HCHO columns and water availability, with high HCHO columns occurring under dry conditions where high LAI dominates (Fig. 5). Most likely, tall vegetation can sustain water stress longer than short vegetation and maintain the secondary metabolism to produce isoprene emissions.

We find that negative trends in AOD lead to decreases in HCHO in all regions, except for India-China ( Table 2). This behavior might be related to the correlation between AOD and anthropogenic non-methane VOC (NMVOC) emissions in many regions. Our result is therefore consistent with the positive/negative trends in HCHO associated to increasing/decreasing trends in anthropogenic emissions (De Smedt et al., 2010, 2015; Zhu et al., 2017). On the other hand, however, the decrease in AOD leads to higher solar radiation (regional brightening), which should result in increased HCHO columns, as we find across India-China, where the reduction in AOD leads to enhanced HCHO columns. Across China, a modeling study using the NASA ModelE2-YIBs global Earth system model showed that anthropogenic aerosols drive decreases in isoprene emissions due to aerosol-induced reductions in direct radiation (Strada and Unger, 2016). However, given that radiation can contribute to the formation or destruction of HCHO, the assessment of the relationship between HCHO and radiation (of which AOD is a proxy) is problematic (e.g. Zheng et al., 2015).

Cross sectional plots indicate a negative spatial correlation between HCHO columns and precipitation, except for Australia (Fig. 4). Although wet deposition does not affect HCHO columns, previous studies found a negative correlation with precipitation over the tropics in the boreal autumn (Zheng et al., 2015) and over highly polluted regions (Báez et al., 1993). It is also possible that high precipitation prevents biomass burning, thus reducing pyrogenic sources of HCHO, and reduces temperatures and resulting HCHO columns over temperate areas, where precipitation and temperatures tend to be negatively correlated (Trenberth and Shea, 2005).

Across the Amazon Basin region and Europe, declining HCHO columns over time are negatively correlated with drying trends in soil moisture and SPEI, respectively ( Table 2), indicating that biogenic emissions may increase under water stress conditions. Over the Amazon Basin region, the spatial relationship between HCHO columns and water availability also suggests that dry conditions favor high HCHO columns, and this effect is stronger in regions with low soil moisture (Fig. 4.(b). This result agrees with Fig. 6.b and Table 2) indicating, based on temporal relationships, that a negative temporal trend in soil moisture has a positive effect on HCHO columns. For Europe and especially the Mediterranean region, this result agrees with findings from an experiment performed at the O3HP site (Oak Observatory at the Observatoire de Haute Provence) in southern France in 2012–2013 (Genard-Zielinski et al., 2014, 2015, 2018), which focused on the effects of simulated drought on a single Mediterranean species (*Quercus pubescens*). Under natural drought, the drought-adapted species *Q. pubescens* limited evapotranspiration and maintained or amplified isoprene emissions to protect plant membranes, while, under amplified drought, isoprene emissions exponentially decreased with soil water content. Our statistical models detected effects of natural drought on isoprene emissions only via SPEI, likely because this indicator depends on temperature and precipitation, which are extremely high and low, respectively, during drought conditions (Vicente-Serrano et al., 2010). This finding may explain the role of SPEI in our statistical models for reproducing the 2015 peak in European HCHO columns under heatwave conditions (Fig. S.3).

## 5. Conclusions

Using space retrievals of HCHO column concentrations as a surrogate for isoprene emissions, we investigated the relationship between isoprene emissions and drivers of global change at large spatio-temporal scales over the period 2005–2016. We found regional temporal trends in HCHO columns, and specifically decreases across Europe, Amazon, southern Africa, and southern Australia, and increases across India-China, supporting findings from previous studies (De Smedt et al., 2010, 2015). Analysis of these trends revealed temporal variations in impacts of single and combined drivers (temperature, precipitation, soil moisture, drought index, biomass, aerosols, and burned fraction) on HCHO columns across the study period, at global and regional scales. In general, HCHO columns are positively related with temperature at the global scale and across the Amazon Basin and India-China regions, with HCHO columns increasing with temperature even under low precipitation, provided that the levels of soil moisture are sufficient to sustain vegetation function and isoprene emissions. The role of water availability and water stress in HCHO columns varies regionally. Water availability sustains isoprene emissions in dry regions such as Australia, where HCHO columns are negatively associated with temperature and positively associated with precipitation. In contrast, HCHO columns are negatively sensitive to trends in soil moisture levels across the Amazon and SPEI over Europe (drier conditions lead to greater columns of HCHO).

We chose a statistical approach that (a) simultaneously assesses the contribution of different drivers of global change on trends in HCHO columns; and (b) explicitly accounts for the role of water availability using multiple predictors related to this driver (i.e., precipitation, soil moisture and drought index). Using this approach, our results: (1) suggest the importance of water availability in sustaining the positive relation between isoprene emissions and temperature, (2) confirm the contrasting effects of water stress on isoprene emissions, with regions where drier conditions enhance isoprene emissions (i.e., Europe and the Amazon Basin) and others where water availability sustains isoprene emissions under hot conditions (i.e., Australia). These different behaviors appear to support the thesis of Peñuelas and Staudt (2010) that mild/short-term water stress amplifies or maintains isoprene emissions, while severe/long water stress reduces isoprene emissions. In addition, these findings suggest that the effect of water stress on isoprene emissions differs from one region to another. Using OMI HCHO columns over the South-Eastern United States, Wang et al. (2022) found that HCHO is 6% higher during mild drought and 23% during severe droughts. These results support future developments in biogenic emission models to implement algorithms able to reproduce both regimes (mild/short water stress, increasing emissions; severe/long water stress, decreasing emissions) and different vegetation/region sensitivity to water stress. Recently, Wang et al. (2021) tested a parameterization which increases isoprene emissions under mild water stress via changes in leaf temperature. When applied over China, this parameterization increases isoprene emissions up to 30%. However, at the global scale the impacts of water stress on isoprene emissions remain unclear, and across some regions (i.e., Australia) the unknown contributions of the applied statistical models remain large, suggesting that the models do not entirely reproduce the observed trend in HCHO columns. Further analysis is required using longer satellite time series, attempting to separate the contribution to formaldehyde columns from isoprene and terpenes, which show a different behavior under water stress (Peñuelas and Staudt, 2010; Bonn et al., 2019), trying to account for different NOx regimes to better estimate "background HCHO formation" (Wolfe et al., 2016), and including predictors of NMVOC to filter out the contribution from anthropogenic sources to HCHO columns. Wolfe et al. (2016) report that a decrease of NOx emissions by a factor of 2 would lead to reduced HCHO columns by about 30%. Long-term records of satellite OMI $NO_2$ column data could be included as an additional predictor in our modeling framework in future work. Moreover, to filter out the contribution from anthropogenic sources to HCHO columns, we could include predictors of non-methane VOC sources, e.g. global anthropogenic NMVOC emission inventories from e.g. the Copernicus Atmosphere Monitoring Service (CAMS-GLOB-ANT, Granier et al., 2019; Elguindi et al., 2020) or the Community Emissions Data System (CEDS; Hoesly et al., 2019). Note, however, that the estimated trends in bottom-up inventories have large uncertainties, especially in regions undergoing fast population and/or policy changes and where accurate information is either absent or limited (Bauwens et al., 2022). In the future, the availability of high resolution HCHO columns (De Smedt et al., 2021) and next-generation machine learning isoprene retrievals (Wells et al., 2022), together with longer time-series of soil moisture data from different datasets (e.g., the NASA Soil Moisture Active Passive instrument and the European Space Agency Soil Moisture and Ocean Salinity mission) will provide new opportunities to improve our understanding of the role of water availability in the isoprene production and emission.

## CRediT authorship contribution statement

**S. Strada:** Designed the article, Performed the observation analysis, Writing – original draft. **M. Fernández-Martínez:** Designed the article, Performed the observation analysis, Writing – original draft. **J. Peñuelas:** Designed the article, Writing – original draft. **M. Bauwens:** Writing – original draft. **T. Stavrakou:** Writing – original draft. **A. Verger:** Writing – original draft. **F. Giorgi:** Writing – original draft.

## Declaration of competing interest

The authors declare the following financial interests/personal relationships which may be considered as potential competing interests: Strada Susanna reports financial support, article publishing charges, and travel were provided by European Commission.

## Data availability

Data will be made available on request.

## Acknowledgments

The data that support the findings of this study were derived from the following resources available in the public domain: (a) formaldehyde column concentrations from the Ozone Monitoring Instrument as produced by the EU FP7 project Quality Assurance for Essential Climate Variables (FP7-SPACE-2103-1, Project No 607405; http://www.qa4ecv.eu), (b) surface temperature and precipitation from the CRU-TS v4.03 dataset made available under the Open Database License by the University of East Anglia (https://sites.uea.ac.uk/cru/data/), (c) the root-zone soil moisture from the Global Land Evaporation Amsterdam Model v3.3b (https://www.gleam.eu/), (d) the Standardized Precipitation-Evapotranspiration Index v2.6 (https://spei.csic.es/spei_database), (e) the Leaf Area Index from the Copernicus Global Land Service (CGLOPS-1, 199494-JRC) (https://land.copernicus.eu/global/products/lai), (f) the Aerosol Optical Depth from the Moderate Resolution Imaging Spectroradiometer available at the NASA Goddard Space Flight Center and the Atmosphere Archive and Distribution System Distributed Active Archive Center (https://ladsweb.modaps.eosdis.nasa.gov/), and (h) the burned fraction from the Global Fire Emissions Database (https://www.globalfiredata.org/). Any rights in individual contents of the SPEI and CRU-TS database are licensed under the Database Contents License.

This work represents a contribution to the CSIC Thematic Interdisciplinary Platform TELEDETECT.

This project has received funding from the European Union's Horizon 2020 research and innovation programme under grant agreement No.: 791413 (project IDIOM2). Financial support, article publishing charges and travel were provided by the H2020 Marie Skłodowska-Curie Actions programme.

## Appendix A. Supplementary data

Supplementary material related to this article can be found online at https://doi.org/10.1016/j.atmosenv.2022.119530.

## References

Aragão, L.E.O.C., Anderson, L.O., Fonseca, M.G., Rosan, T.M., Vedovato, L.B., Wagner, F.H., Silva, C.V.J., Silva Junior, C.H.L., Arai, E., Aguiar, A.P., Barlow, J., Berenguer, E., Deeter, M.N., Domingues, L.G., Gatti, L., Gloor, M., Malhi, Y., Marengo, J.A., Miller, J.B., Phillips, O.L., Saatchi, S., 2018. 21St century drought-related fires counteract the decline of Amazon deforestation carbon emissions. Nature Commun. 9 (1), 536. http://dx.doi.org/10.1038/s41467-017-02771-y.

Atkinson, R., Arey, J., 2003. Gas-phase tropospheric chemistry of biogenic volatile organic compounds: a review. Atmos. Environ. 37 (2), 197–219. http://dx.doi.org/10.1016/S1352-2310(03)00391-1.

Báez, A., Padilla, H.G., Belmont, R.D., 1993. Scavenging of atmospheric formaldehyde by wet precipitation. Environ. Pollut. 79 (3), 271–275. http://dx.doi.org/10.1016/0269-7491(93)90100-3.

Baldwin, I., 2010. Plant volatiles. Curr. Biol. 20 (9).

Bauwens, M., Stavrakou, T., Müller, J.F., De Smedt, I., Van Roozendael, M., Van Der Werf, G.R., Wiedinmyer, C., Kaiser, J.W., Sindelarova, K., Guenther, A., 2016. Nine years of global hydrocarbon emissions based on source inversion of OMI formaldehyde observations. Atmos. Phys. Chem. 16, 10133–10158. http://dx.doi.org/10.5194/acp-16-10133-2016.

Bauwens, M., Verreyken, B., Stavrakou, T., Müller, J.-F., De Smedt, I., 2022. Spaceborne evidence for significant anthropogenic VOC trends in Asian cities over 2005–2019. Environ. Res. Lett. 17 (1), 015008. http://dx.doi.org/10.1088/1748-9326/ac46eb.

Beguería, S., Vicente-Serrano, S., Reig, F., Latorre, B., 2014. Standardized precipitation evapotranspiration index (SPEI) revisited: parameter fitting, evapotranspiration models, kernel weighting, tools, datasets and drought monitoring. Int. J. Climatol. 34, 3001–3023.

Bonn, B., Magh, R.-K., Rombach, J., Kreuzwieser, J., 2019. Biogenic isoprenoid emissions under drought stress: different responses for isoprene and terpenes. Biogeosciences 16, 4627–4645. http://dx.doi.org/10.5194/bg-16-4627-201.

Brasseur, G.P., Jacob, D.J., 2017. Mathematical Modeling of Atmospheric Chemistry. Cambridge University Press, p. 606, chapter 11.

Bürgi, M., Schuler, A., 2003. Driving forces of forest management - an analysis of regeneration practices in the forests of the Swiss central plateau during the 19th and 20th century. Forest Ecol. Manag. 176, 173–183. http://dx.doi.org/10.1016/S0378-1127(02)00270-0.

Chameides, W.L., Lindsay, R.W., Richardsen, J., Kiang, C.S., 1988. The role of biogenic hydrocarbons in urban photochemical smog: Atlanta as a case study. Science 241, 1473–1475. http://dx.doi.org/10.1126/science.3420404.

Chen, W.H., Guenther, A.B., Wang, X.M., Chen, Y.H., Gu, D.S., Chang, M., Zhou, S.Z., Wu, L.L., Zhang, Y.Q., 2018. Regional to global biogenic Isoprene emission responses to changes in vegetation from 2000 to 2015. J. Geophys. Res.: Atmos. 123 (7), 3757–3771. http://dx.doi.org/10.1002/2017JD027934.

Churkina, G., Kuik, F., Bonn, B., Lauer, A., Grote, R., Tomiak, K., Butler, T.M., 2017. Effect of VOC emissions from vegetation on air quality in Berlin during a heatwave. Environ. Sci. Technol. 51 (11), 6120–6130. http://dx.doi.org/10.1021/acs.est.6b06514.

Curci, G., Palmer, P.I., Kurosu, T.P., Chance, K., Visconti, G., 2010. Estimating European volatile organic compound emissions using satellite observations of formaldehyde from the Ozone monitoring instrument. Atmos. Chem. Phys. 10 (23), 11501–11517. http://dx.doi.org/10.5194/acp-10-11501-2010.

Dai, A., 2013. Increasing drought under global warming in observations and models. Nature Clim. Change 3, 52–58. http://dx.doi.org/10.1038/nclimate1633.

De Smedt, I., Pinardi, G., Vigouroux, C., Compernolle, S., Bais, A., Benavent, N., Boersma, F., Chan, K.-L., Donner, S., Eichmann, K.-U., Hedelt, P., Hendrick, F., Irie, H., Kumar, V., Lambert, J.-C., Langerock, B., Lerot, C., Liu, C., Loyola, D., Piters, A., Richter, A., Rivera Cárdenas, C., Romahn, F., Ryan, R.G., Sinha, V., Theys, N., Vlietinck, J., Wagner, T., Wang, T., Yu, H., Van Roozendael, M., 2021. Comparative assessment of TROPOMI and OMI formaldehyde observations and validation against MAX-DOAS network column measurements. Atmos. Chem. Phys. 21 (16), 12561–12593. http://dx.doi.org/10.5194/acp-21-12561-2021.

De Smedt, I., Stavrakou, T., Hendrick, F., Danckaert, T., Vlemmix, T., Pinardi, G., Theys, N., Lerot, C., Gielen, C., Vigouroux, C., Hermans, C., Fayt, C., Veefkind, P., Müller, J.-F., Van Roozendael, M., 2015. Diurnal, seasonal and long-term variations of global formaldehyde columns inferred from combined OMI and GOME-2 observations. Atmos. Chem. Phys. 15, 12519–12545. http://dx.doi.org/10.5194/acp-15-12519-2015.

De Smedt, I., Stavrakou, T., Müller, J., van der A, R.J., Van Roozendael, M., 2010. Trend detection in satellite observations of formaldehyde tropospheric columns. Geophys. Res. Lett. 37, http://dx.doi.org/10.1029/2010GL044245.

De Smedt, I., Theys, N., Yu, H., Danckaert, T., Lerot, C., Compernolle, S., Van Roozendael, M., Richter, A., Hilboll, A., Peters, E., Pedergnana, M., Loyola, D., Beirle, S., Wagner, T., Eskes, H., van Geffen, J., Boersma, K.F., Veefkind, P., 2018. Algorithm theoretical baseline for formaldehyde retrievals from S5P TROPOMI and from the QA4ECV project. Atmos. Meas. Tech. 11, 2395–2426. http://dx.doi.org/10.5194/amt-11-2395-2018.

Dorigo, W., Wagner, W., Albergel, C., Albrecht, F., Balsamo, G., Brocca, L., Chung, D., Ertl, M., Forkel, M., Gruber, A., Haas, E., Hamer, P.D., Hirschi, M., Ikonen, J., de Jeu, R., Kidd, R., Lahoz, W., Liu, Y.Y., Miralles, D., Mistelbauer, T., Nicolai-Shaw, N., Parinussa, R., Pratola, C., Reimer, C., van der Schalie, R., Seneviratne, S.I., Smolander, T., Lecomte, P., 2017. ESA CCI soil moisture for improved earth system understanding: State-of-the art and future directions. Remote Sens. Environ. 203, 185–215. http://dx.doi.org/10.1016/j.rse.2017.07.001.

Elguindi, N., Granier, C., Stavrakou, T., Darras, S., Bauwens, M., Cao, H., Chen, C., Denier van Der Gon, H.A.C.D., Dubovik, O., Fu, T.M.M., Henze, D.K.K., Jiang, Z., Keita, S., Kuenen, J.J.P., Kurokawa, J., Liousse, C., Miyazaki, K., Müller, J.F., Qu, Z., Solmon, F., Zheng, B., 2020. Intercomparison of magnitudes and trends in anthropogenic surface emissions from bottom-up inventories, top-down estimates, and emission scenarios. Earths Fut. 8 (8), http://dx.doi.org/10.1029/2020EF001520.

Emmerson, K.M., Palmer, P.I., Thatcher, M., Haverd, V., Guenther, A.B., 2019. Sensitivity of isoprene emissions to drought over south-eastern Australia: Integrating models and satellite observations of soil moisture. Atmos. Environ. (ISSN: 1352-2310) 209, 112–124. http://dx.doi.org/10.1016/j.atmosenv.2019.04.038.

Feng, Z., Yuan, X., Fares, S., Loreto, F., Li, P., Hoshika, Y., Paoletti, E., 2019. Isoprene is more affected by climate drivers than monoterpenes: A meta-analytic review on plant isoprenoid emissions. Plant Cell Environ. 42, 1939–1949. http://dx.doi.org/10.1111/pce.13535.

Fernández-Martínez, M., Sardans, J., Chevallier, F., Ciais, P., Obersteiner, M., Vicca, S., Canadell, J.G., Bastos, A., Friedlingstein, P., Sitch, S., Piao, S.L., Janssens, I.A., Peñuelas, J., 2019. Global trends in carbon sinks and their relationships with $CO_2$ and temperature. Nature Clim. Change 9 (1), 73–79. http://dx.doi.org/10.1038/s41558-018-0367-7.

Fernández-Martínez, M., Vicca, S., Janssens, I.A., Ciais, P., Obersteiner, M., Bartrons, M., Sardans, J., Verger, A., Canadell, J.G., Chevallier, F., Wang, X., Bernhofer, C., Curtis, P.S., Gianelle, D., Grünwald, T., Heinesch, B., Ibrom, A., Knohl, A., Laurila, T., Law, B.E., Limousin, J.M., Longdoz, B., Loustau, D., Mammarella, I., Matteucci, G., Monson, R.K., Montagnani, L., Moors, E.J., Munger, J.W., Papale, D., Piao, S.L., Peñuelas, J., 2017. Atmospheric deposition, $CO_2$, and change in the land carbon sink. Sci. Rep. 7 (1), 9632. http://dx.doi.org/10.1038/s41598-017-08755-8.

Franco, B., Marais, E.A., Bovy, B., Bader, W., Lejeune, B., Roland, G., Servais, C., Mahieu, E., 2016. Diurnal cycle and multi-decadal trend of formaldehyde in the remote atmosphere near 46°N. Atmos. Chem. Phys. 16, 4171–4189. http://dx.doi.org/10.5194/acp-16-4171-2016.

Fuster, B., Sánchez-Zapero, J., Camacho, F., García-Santos, V., Verger, A., Lacaze, R., Weiss, M., Baret, F., Smets, B., 2020. Quality assessment of PROBA-v LAI, fAPAR and fCOVER collection 300 m products of Copernicus global land service. Remote Sens. (ISSN: 2072-4292) 12 (6), http://dx.doi.org/10.3390/rs12061017.

Genard-Zielinski, A.-C., Boissard, C., Fernandez, C., Kalogridis, C., Lathière, J., Gros, V., Bonnaire, N., Ormeño, E., 2015. Variability of BVOC emissions from a mediterranean mixed forest in southern France with a focus on Quercus pubescens. Atmos. Chem. Phys. 15, 431–446. http://dx.doi.org/10.5194/acp-15-431-2015.

Genard-Zielinski, A.-C., Boissard, C., Ormeño, E., Lathière, J., Reiter, I.M., Wortham, H., Orts, J.-P., Temine-Roussel, B., Guenet, B., Bartsch, S., Gauquelin, T., Fernandez, C., 2018. Seasonal variations of Quercus pubescens isoprene emissions from an in natura forest under drought stress and sensitivity to future climate change in the Mediterranean area. Biogeosciences 15, 4711–4730. http://dx.doi.org/10.5194/bg-15-4711-2018.

Genard-Zielinski, A.-C., Ormeño, E., Boissard, C., Fernandez, C., 2014. Isoprene emissions from Downy Oak under water limitation during an entire growing season: What cost for growth? PLoS One 9, http://dx.doi.org/10.1371/journal.pone.0112418.

Giglio, L., Randerson, J.T., van der werf, G.R., 2013. Analysis of daily, monthly, and annual burned area using the fourth-generation global fire emissions database (GFED4). J. Geophys. Res.-Biogeo. 118 (1), 317–328. http://dx.doi.org/10.1002/jgrg.20042.

Granier, C., Darras, S., Denier van Der Gon, H., Jana, D., Elguindi, N., et al., 2019. The Copernicus Atmosphere Monitoring Service global and regional emissions. Technical Report, Copernicus Atmosphere Monitoring Service.

Guenther, A.B., Jiang, X., Heald, C.L., Sakulyanontvittaya, T., Duhl, T., Emmons, L.K., Wang, X., 2012. The model of emissions of gases and aerosols from nature version 2.1 (MEGAN2.1): an extended and updated framework for modeling biogenic emissions. Geosci. Model Dev. 5, 1471–1492. http://dx.doi.org/10.5194/gmd-5-1471-2012.

Harris, I., Osborn, T.J., Jones, P., Lister, D., 2020. Version 4 of the CRU TS monthly high-resolution gridded multivariate climate dataset. Sci. Data 7 (1), 109. http://dx.doi.org/10.1038/s41597-020-0453-3.

Hartmann, D., Klein Tank, A., Rusticucci, M., Alexander, L., Brönnimann, S., Charabi, Y., Dentener, F., Dlugokencky, E., Easterling, D., Kaplan, A., Soden, B., Thorne, P., Wild, M., Zhai, P., 2003. Climate change 2013: The physical science basis. In: Stocker, T., Qin, D., Plattner, G.-K., Tignor, M., Allen, S., Boschung, J., Nauels, A., Xia, Y., Bex, V., Midgley, P. (Eds.), Contribution of Working Group I to the Fifth Assessment Report of the Intergovernmental Panel on Climate Change. Cambridge University Press.

Hilker, T., Lyapustin, A.I., Tucker, C.J., Hall, F.G., Myneni, R.B., Wang, Y., Bi, J., Mendes de Moura, Y., Sellers, P.J., 2014. Vegetation dynamics and rainfall sensitivity of the Amazon. Proc. Natl. Acad. Sci. (ISSN: 0027-8424) 111 (45), 16041–16046. http://dx.doi.org/10.1073/pnas.1404870111.

Hoesly, R., O'Rourke, P., Braun, C., Feng, L., Smith, S.J., Pitkanen, T., Siebert, J., Vu, L., Presley, M., Bolt, R., Goldstein, B., Kholod, N., 2019. CEDS: Community Emissions Data System (Version Dec-23-2019). Zenodo, http://dx.doi.org/10.5281/zenodo.3592073.

Jia, G., Shevliakova, E., Artaxo, P., De Noblet-Ducoudré, N., Houghton, R., House, J., Kitajima, K., Lennard, C., Popp, A., Sirin, A., Sukumar, R., Verchot, L., 2019. In: Shukla, P., Skea, J., Buendia, E.C., Masson-Delmotte, V., Pörtner, H.-O., Roberts, D., Zhai, P., Slade, R., Connors, S., van Diemen, R., Ferrat, M., Haughey, E., Luz, S., Neogi, S., Pathak, M., Petzold, J., Pereira, J.P., Vyas, P., Huntley, E., Kissick, K., Belkacemi, M., Malley, J. (Eds.), Climate Change and Land: an IPCC special report on climate change, desertification, land degradation, sustainable land management, food security, and greenhouse gas fluxes in terrestrial ecosystems.

Kesselmeier, J., Staudt, M., 1999. Biogenic volatile organic compounds (VOC): An overview on emission, physiology and ecology. J. Atm. Chem. 33, 23–88.

Komsta, L., 2012. Mblm: Median-based linear models.

Langner, J., Engardt, M., Baklanov, A., Christensen, J., Gauss, M., Geels, C., Hedegaard, G., Simpson, D., Soares, J., Sofiev, M., Wind, P., Zakey, A., 2012. A multi-model study of impacts of climate change on surface ozone in europe. Atmos. Chem. Phys. 12, 10423–10440. http://dx.doi.org/10.5194/acp-12-10423-2012.

Laothawornkitkul, J., Taylor, J.E., Paul, N.D., Hewitt, C.N., 2009. Biogenic volatile organic compounds in the earth system. New Phytol. 183, 27–51. http://dx.doi.org/10.1111/j.1469-8137.2009.02859.x.

Levelt, P., van den Oord, G., Dobber, M., Malkki, A., Visser, H., de Vries, J., Stammes, P., Lundell, J.O., Saari, H., 2006. The Ozone monitoring instrument. IEEE Trans. Geosci. Remote Sens. 44, 1093–1101.

Levy, R.C., Mattoo, S., Munchak, L.A., Remer, L.A., Sayer, A.M., Patadia, F., Hsu, N.C., 2013. The collection 6 MODIS aerosol products over land and ocean. Atmos. Meas. Tech. 6 (11), 2989–3034. http://dx.doi.org/10.5194/amt-6-2989-2013.

Levy, R.C., Remer, L.A., Kleidman, R.G., Mattoo, S., Ichoku, C., Kahn, R., Eck, T.F., 2010. Global evaluation of the collection 5 MODIS dark-target aerosol products over land. Atmos. Chem. Phys. 10 (21), 10399–10420. http://dx.doi.org/10.5194/acp-10-10399-2010.

Martens, B., Miralles, D.G., Lievens, H., Fernández-Prieto, D., Verhoest, N.E.C., 2016. Improving terrestrial evaporationestimates over continental Australia through assimilation of SMOS soil moisture. Int. J. Appl. Earth Obs. 48, 146–162. http://dx.doi.org/10.1016/j.jag.2015.09.012.

Martens, B., Miralles, D.G., Lievens, H., van der Schalie, R., de Jeu, R.A.M., Fernández-Prieto, D., Beck, H.E., Dorigo, W.A., Verhoest, N.E.C., 2017. GLEAM v3: satellite-based land evaporation and root-zone soil moisture. Geosci. Model Dev. 10 (5), 1903–1925. http://dx.doi.org/10.5194/gmd-10-1903-2017.

Meleux, F., Solmon, F., Giorgi, F., 2007. Increase in summer European ozone amounts due to climate change. Atmos. Environ. 41, 7577–7587. http://dx.doi.org/10.1016/j.atmosenv.2007.05.048.

Morfopoulos, C., Müller, J.-F., Stavrakou, T., Bauwens, M., De Smedt, I., Friedlingstein, P., Prentice, I.C., Regnier, P., 2022. Vegetation responses to climate extremes recorded by remotely sensed atmospheric formaldehyde. Global Change Biol. 28 (5), 1809–1822. http://dx.doi.org/10.1111/gcb.15880.

Müller, J.-F., Stavrakou, T., Wallens, S., De Smedt, I., Van Roozendael, M., Potosnak, M.J., Rinne, J., Munger, B., Goldstein, A., Guenther, A.B., 2008. Global isoprene emissions estimated using MEGAN, ECMWF analyses and a detailed canopy environment model. Atmos. Chem. Phys. 8, 1329–1341.

Niinemets, Ü., 2009. Mild versus severe stress and BVOCs: thresholds, priming and consequences. Trends Plant Sci. 15, 145–153. http://dx.doi.org/10.1016/j.tplants.2009.11.008.

Niinemets, Ü., Loreto, F., Reichstein, M., 2004. Physiological and physicochemical controls on foliar volatile organic compound emissions. Trends Plant Sci. 9 (4), 180–186. http://dx.doi.org/10.1016/j.tplants.2004.02.006.

Ohlson, J.A., Kim, S., 2015. Linear valuation without OLS: The Theil-Sen estimation approach. Rev. Account. Stud. 20.

Opacka, B., Müller, J.-F., Stavrakou, T., Bauwens, M., Sindelarova, K., Markova, J., Guenther, A.B., 2021. Global and regional impacts of land cover changes on isoprene emissions derived from spaceborne data and the MEGAN model. Atmos. Chem. Phys. 21 (11), 8413–8436. http://dx.doi.org/10.5194/acp-21-8413-2021.

Orth, R., Zscheischler, J., Seneviratne, S.I., 2016. Record dry summer in 2015 challenges precipitation projections in central Europe. Sci. Rep. 6 (1), 28334. http://dx.doi.org/10.1038/srep28334.

Pacifico, F., Harrison, S.P., Jones, C.D., Sitch, S., 2009. Isoprene emissions and climate. Atmos. Environ. 43, 6121–6135. http://dx.doi.org/10.1016/j.atmosenv.2009.09.002.

Palmer, P.I., Jacob, D.J., Fiore, A.M., Martin, R.V., Chance, K., Kurosu, T.P., 2003. Mapping isoprene emissions over north America using formaldehyde column observations from space. J. Geophys. Res.: Atmos. 108 (D6), http://dx.doi.org/10.1029/2002JD002153.

Peñuelas, J., Llusià, J., 2001. The complexity of factors driving volatile organic compound emissions by plants. Biol. Plantarum 44 (4), 481–487.

Peñuelas, J., Staudt, M., 2010. BVOCs and global change. Trends Plant Sci. 15 (3), 133–144. http://dx.doi.org/10.1016/j.tplants.2009.12.005.

R. Core Team, 2017. R: A Language and Environment for Statistical Computing. R Foundation for Statistical Computing, Vienna, Austria, Available at https://www.R-project.org/.

Randerson, J.T., Chen, Y., van der Werf, G.R., Rogers, B.M., Morton, D.C., 2012. Global burned area and biomass burning emissions from small fires. J. Geophys. Res.-Biogeo. 117 (G4), http://dx.doi.org/10.1029/2012JG002128.

Sánchez, J., Camacho, F., 2017. Quality Assessment Report of LAI, FAPAR, FCover from SPOT/VEGETATION Collection 1km Version 2. Technical report, Copernicus Global Land Operation, Available online at https://land.copernicus.eu/global/sites/cgls.vito.be/files/products/GIOGL1_QAR_LAI1km-VGT-V2_I2.01.pdf.

Shi, Y., Zhang, J., Reid, J.S., Liu, B., Hyer, E.J., 2014. Critical evaluation of cloud contamination in the MISR aerosol products using MODIS cloud mask products. Atmos. Meas. Tech. 7, 1791–1801. http://dx.doi.org/10.5194/amt-7-1791-2014.

Sindelarova, K., Granier, C., Bouarar, I., Guenther, A., Tilmes, S., Stavrakou, T., Müller, J.-F., Kuhn, U., Stefani, P., Knorr, W., 2014. Global data set of biogenic VOC emissions calculated by the MEGAN model over the last 30 years. Atmos. Chem. Phys. 14, 9317–9341. http://dx.doi.org/10.5194/acp-14-9317-2014.

Spinoni, J., Naumann, G., Vogt, J., Barbosa, P., 2015. European drought climatologies and trends based on a multi-indicator approach. Glob. Planet. Change (ISSN: 0921-8181) 127, 50–57. http://dx.doi.org/10.1016/j.gloplacha.2015.01.012.

Stavrakou, T., Müller, J.-F., Bauwens, M., De Smedt, I., Lerot, C., Van Roozendael, M., Coheur, P.-F., Clerbaux, C., Boersma, K.F., van der A., R., Song, Y., 2016. Substantial underestimation of post-harvest burning emissions in the north China plain revealed by multi-species space observations. Sci. Rep. (ISSN: 2045-2322) 6 (1), 32307. http://dx.doi.org/10.1038/srep32307.

Stavrakou, T., Müller, J.-F., Bauwens, M., De Smedt, I., Van Roozendael, M., De Mazière, M., Vigouroux, C., Hendrick, F., George, M., Clerbaux, C., Coheur, P., Guenther, A., 2015. How consistent are top-down hydrocarbon emissions based on formaldehyde observations from GOME-2 and OMI? Atmos. Chem. Phys. 15, 11861–11884. http://dx.doi.org/10.5194/acp-15-11861-2015.

Stavrakou, T., Müller, J.-F., Bauwens, M., De Smedt, I., Van Roozendael, M., Guenther, A., Wild, M., Xia, X., 2014. Isoprene emissions over Asia 1979–2012: impact of climate and land-use changes. Atmos. Chem. Phys. 14 (9), 4587–4605. http://dx.doi.org/10.5194/acp-14-4587-2014.

Stavrakou, T., Müller, J.-F., Bauwens, M., I., D.S., Van Roozendael, M., Guenther, A., 2018. Impact of short-term climate variability on volatile organic compounds emissions assessed using OMI satellite formaldehyde observations. Geophys. Res. Lett. 45, 8681–8689. http://dx.doi.org/10.1029/2018GL078676.

Stavrakou, T., Müller, J.-F., De Smedt, I., Van Roozendael, M., van der Werf, G.R., Giglio, L., Guenther, A., 2009. Global emissions of non-methane hydrocarbons deduced from SCIAMACHY formaldehyde columns through 2003–2006. Atmos. Chem. Phys. 9 (11), 3663–3679. http://dx.doi.org/10.5194/acp-9-3663-2009.

Stokland, J.N., et al., 2003. Forest Biodiversity Indicators in the Nordic Countries. Status Based on National Forest Inventories, Vol. 514. Nordic Council of Ministers.

Strada, S., Unger, N., 2016. Potential sensitivity of photosynthesis and isoprene emission to direct radiative effects of atmospheric aerosol pollution. Atmos. Chem. Phys. 16 (7), 4213–4234. http://dx.doi.org/10.5194/acp-16-4213-2016, URL https://acp.copernicus.org/articles/16/4213/2016/.

Streets, D.G., Yan, F., Chin, M., Diehl, T., Mahowald, N., Schultz, M., Wild, M., Wu, Y., Yu, C., 2009. Anthropogenic and natural contributions to regional trends in aerosol optical depth, 1980–2006. J. Geophys. Res.: Atmos. 114 (D10), http://dx.doi.org/10.1029/2008JD011624.

Taschetto, A.S., Sen Gupta, A., Ummenhofer, C.C., England, M.H., 2016. Can Australian multiyear droughts and wet spells be generated in the absence of oceanic variability? J. Clim. 29 (17), 6201–6221. http://dx.doi.org/10.1175/JCLI-D-15-0694.1.

Trenberth, K.E., Shea, D.J., 2005. Relationships between precipitation and surface temperature. Geophys. Res. Lett. 32 (14), http://dx.doi.org/10.1029/2005GL022760.

Unger, N., Harper, K., Zheng, Y., Kiang, N.Y., Aleinov, I., Arneth, A., Schurgers, G., Amelynck, C., Goldstein, A., Guenther, A., Heinesch, B., Hewitt, C.N., Karl, T., Laffineur, Q., Langford, B., McKinney, K.A., Misztal, P., Potosnak, M., Rinne, J., Pressley, S., Schoon, N., Serça, D., 2013. Photosynthesis-dependent isoprene emission from leaf to planet in a global carbon–chemistry–climate model. Atmos. Chem. Phys. 13, 10243–10269. http://dx.doi.org/10.5194/acp-13-10243-2013.

Unger, N., Yue, X., Harper, K.L., 2017. Aerosol climate change effects on land ecosystem services. Faraday Discuss. 200, 121–142. http://dx.doi.org/10.1039/C7FD00033B.

Verger, A., Baret, F., Weiss, M., 2014. Near real-time vegetation monitoring at global scale. IEEE J. Sel. Top. Appl. Earth Obs. Remote Sens. 7 (8), 3473–3481. http://dx.doi.org/10.1109/JSTARS.2014.2328632.

Verger, A., Baret, F., Weiss, M., 2019. Algorithm Theoretical Basis Document of Leaf Area Index (LAI), Fraction of Absorbed Photosynthetically Active Radiation (FAPAR), Fraction of green Vegetation Cover (FCover) Collection 1km Version 2. Technical report, Copernicus Global Land Operation, Available online at https://land.copernicus.eu/global/sites/cgls.vito.be/files/products/CGLOPS1_ATBD_LAI1km-V2_I1.41.pdf.

Vicente-Serrano, S., Beguería, S., López-Moreno, J.I., 2010. A multi-scalar drought index sensitive to global warming: The standardized precipitation evapotranspiration index - SPEI. J. Clim. 23, 1696–1718.

Vicente-Serrano, S.M., Lopez-Moreno, J.-I., Beguería, S., Lorenzo-Lacruz, J., Sanchez-Lorenzo, A., García-Ruiz, J.M., Azorin-Molina, C., Morán-Tejeda, E., Revuelto, J., Trigo, R., Coelho, F., Espejo, F., 2014. Evidence of increasing drought severity caused by temperature rise in southern Europe. Environ. Res. Lett. 9 (4), 044001. http://dx.doi.org/10.1088/1748-9326/9/4/044001.

Wang, Y., Lin, N., Li, W., Guenther, A., Lam, J.C.Y., Tai, A.P.K., Potosnak, M.J., Seco, R., 2022. Satellite-derived constraints on the effect of drought stress on biogenic isoprene emissions in the southeastern US. Atmos. Chem. Phys. 22 (21), 14189–14208. http://dx.doi.org/10.5194/acp-22-14189-2022.

Wang, H., Wu, Q., Guenther, A.B., Yang, X., Wang, L., Xiao, T., Li, J., Feng, J., Xu, Q., Cheng, H., 2021. A long-term estimation of biogenic volatile organic compound (BVOC) emission in China from 2001–2016: the roles of land cover change and climate variability. Atmos. Chem. Phys. 21 (6), 4825–4848. http://dx.doi.org/10.5194/acp-21-4825-2021.

Wells, K.C., Millet, D.B., Payne, V.H., Vigouroux, C., Aquino, C.A.B., De Mazière, M., de Gouw, J.A., Graus, M., Kurosu, T., Warneke, C., Wisthaler, A., 2022. Next-generation Isoprene measurements from space: Detecting daily variability at high resolution. J. Geophys. Res.: Atmos. 127 (5), http://dx.doi.org/10.1029/2021JD036181, e2021JD036181, e2021JD036181 2021JD036181.

Wild, M., 2009. Global dimming and brightening: A review. J. Geophys. Res.: Atmos. 114 (D10), http://dx.doi.org/10.1029/2008JD011470.

Wild, M., 2012. Enlightening global dimming and brightening. BAMS 93 (1), 27–37. http://dx.doi.org/10.1175/BAMS-D-11-00074.1.

Wolfe, G.M., Kaiser, J., Hanisco, T.F., Keutsch, F.N., de Gouw, J.A., Gilman, J.B., Graus, M., Hatch, C.D., Holloway, J., Horowitz, L.W., Lee, B.H., Lerner, B.M., Lopez-Hilifiker, F., Mao, J., Marvin, M.R., Peischl, J., Pollack, I.B., Roberts, J.M., Ryerson, T.B., Thornton, J.A., Veres, P.R., Warneke, C., 2016. Formaldehyde production from isoprene oxidation across $NO_x$ regimes. Atmos. Chem. Phys. 16 (4), 2597–2610. http://dx.doi.org/10.5194/acp-16-2597-2016.

Yáñez-Serrano, A.M., Bourtsoukidis, E., Alves, E.G., Bauwens, M., Stavrakou, T., Llusià, J., Filella, I., Guenther, A., Williams, J., Artaxo, P., Sindelarova, K., Doubalova, J., Kesselmeier, J., Peñuelas, J., 2020. Amazonian biogenic volatile organic compounds under global change. Global Change Biol. 26 (9), 4722–4751. http://dx.doi.org/10.1111/gcb.15185.

Yue, X., Unger, N., Zheng, Y., 2015. Distinguishing the drivers of trends in land carbon fluxes and plant volatile emissions over the past 3 decades. Atmos. Chem. Phys. 15 (20), 11931–11948. http://dx.doi.org/10.5194/acp-15-11931-2015.

Zheng, Y., Unger, N., Barkley, M.P., Yue, X., 2015. Relationships between photosynthesis and formaldehyde as a probe of isoprene emission. Atmos. Chem. Phys. 15 (15), 8559–8576. http://dx.doi.org/10.5194/acp-15-8559-2015.

Zhu, L., Mickley, L.J., Jacob, D.J., Marais, E.A., Sheng, J., Hu, L., Abad, G.G.G., Chance, K., 2017. Long-term (2005–2014) trends in formaldehyde (HCHO) columns across north America as seen by the OMI satellite instrument: Evidence of changing emissions of volatile organic compounds. Geophys. Res. Lett. 44 (13), 7079–7086. http://dx.doi.org/10.1002/2017GL073859.